

Energy Aware Impedance Control of a Flying End-effector in the Port-Hamiltonian Framework

Ramy Rashad, Davide Bicego, Jelle Zult, Santiago Sanchez-Escalonilla, Ran Jiao, Antonio Franchi, *Senior Member, IEEE*, Stefano Stramigioli, *Fellow, IEEE*

Abstract—The extension of variable stiffness impedance control for safe wrench regulation using the concept of energy tanks is tackled in this paper, where both the modeling and the control are carried out in the port Hamiltonian framework. We exploit previous well-known results in the literature of ground manipulators and extend them to be applied for novel and challenging aerial physical interaction applications. The energy-awareness of the presented control method guarantees the stability of the aerial robot in both free-flight and in-contact scenarios together with a level of safety in the case of contact-loss with the unknown environment. To the best of our knowledge, this is the first time an energy-based impedance controller for aerial robots is derived, extended to accomplish interaction control, enhanced to account for safety behavior entirely in the port-Hamiltonian framework, and extensively tested with real experiments on a fully-actuated multirotor aerial vehicle.

Index Terms—Energy-aware robotics, impedance control, port-Hamiltonian systems, aerial physical interaction, energy-tanks.

I. INTRODUCTION

In recent years there has been an exploding interest within the aerial robotics community for extending the current applications of multirotor aerial vehicles (MAVs) to those that require aerial physical interaction. Most of the currently successful applications are exploiting MAVs to only observe the environment and sense it remotely. However, there have been many research efforts in the past two decades to enable MAVs to physically interact with their environment, and thus acts as flying manipulators instead of flying sensors.

This work has been partially funded by the cooperation program “IN-TERREG Deutschland-Nederland” as part of the SPECTORS project number 143081, the PortWings project funded by the European Research Council [grant agreement No. 787675], and the European Union’s Horizon 2020 research and innovation programme [grant agreement No. 871479] AERIAL-CORE.

R. Rashad and D. Bicego are with the Robotics and Mechatronics group, Faculty of Electrical Engineering, Mathematics and Computer Science, University of Twente, Enschede, The Netherlands. Email: {r.a.m.rashadhashem,d.bicego}@utwente.nl

J. Zult is with Bond High Performance 3D Technology, Enschede, The Netherlands. Email: jdzult@gmail.com

S. Sanchez-Escalonilla is with the Faculty of Science and Engineering, University of Groningen, Groningen, The Netherlands. Email: santiago.sanchez@rug.nl

R. Jiao is with the School of Mechanical Engineering and Automation, Beihang University, Beijing, China. Email: jiaoran@buaa.edu.cn

A. Franchi is with the Robotics and Mechatronics group, University of Twente, and LAAS-CNRS, Université de Toulouse, CNRS, Toulouse, France. Email: a.franchi@utwente.nl

S. Stramigioli is with the Robotics and Mechatronics group, University of Twente, and ITMO University, Saint Petersburg, Russia. Email: s.stramigioli@utwente.nl

Manuscript received May 24, 2021

Enticed by the numerous potential applications of flying manipulators, many research groups and civilian companies have contributed to advancing the field of aerial physical interaction. Consequently, many synergies have been established worldwide in the past years with the aim of creating flying manipulators such as the EU projects: AIROBOTS, AR-CAS, AEROWORKS, AEROARMS, AEROBI, SPECTORS, HYFLIERS, and AERIAL-CORE, to mention a few.

One common approach for realizing a flying-manipulator is the use of fully-actuated MAVs that have non-parallel propellers allowing for controlling all six degrees of freedom of the aerial robot. In this physical interaction paradigm, the MAV itself is considered as a **flying end-effector** which can interact with its environment [1]. Compared to other approaches in the literature, such as endowing a conventional MAV with a robotic manipulator arm as in [2, 3], a flying end-effector is mechanically simpler, more robust, and capable of applying higher lateral forces.

In this work, we focus on the design of a control system suitable for aerial physical interaction using a flying end-effector. Compared to the motion controllers widely used for MAVs, the design of an interaction controller is fundamentally different and has numerous challenges. First, the primary control objective for conventional MAVs is to achieve stability in free-flight and to reject external disturbances to maximize performance. However for a flying end-effector, in addition to free-flight stability, it should be able to interact with and exert forces on an unknown environment in a stable manner.

Second, the closed-loop stability of a flying end-effector physically interacting with its environment depends on the dynamics of the aerial robot’s physics, its controller, as well as the environment. In general, the overall system dynamics are unknown and could also be discontinuous in an interaction scenario with contact/non-contact situations. Therefore, the environment should be part of the stability analysis conducted during contact. In the traditional framework of analyzing the closed-loop dynamical system as an isolated *closed system*, certain assumptions are made to incorporate a model of the environment such as using linear springs and dampers. However, such unrealistic and simplistic models only guarantee contact stability for very specific and limited types of real environments.

Third, the traditional framework of modeling a dynamical system using block diagrams, based on unilateral signals, is not suitable for modeling and control of a flying end-effector. In free-flight operation, the output signal of the robot is considered as its pose (i.e., combined position and orientation)

which is regulated by a pose controller, whereas in contact operation, the pose of the robot can no longer be controlled as it is constrained by the environment. Moreover, if an additional wrench (i.e., combined force and torque) controller is used to regulate the interaction wrench between the robot and the environment during contact, such wrench can no longer be regulated once the robot loses contact and is in a free-flight situation. Therefore, hybrid pose-wrench control techniques, e.g., [4], are ill-suited for interactive aerial robots as they require perfect knowledge of the environment and the occurrence of contact, which is not practical for unstructured and unknown environments. Due to the aforementioned challenges, a different paradigm for modeling, analysis, and control is needed for this class of aerial robots.

In this work, we address the aerial physical interaction problem using the port-Hamiltonian paradigm where the flying end-effector is modeled as an *open system* that can be interconnected to any environment via a power port. By designing controllers that guarantee that the closed loop system fulfills certain requirements as seen from this environment port, the contact stability can be asserted independently of any environment model [5]. Thus, we do not aim to either control the pose or wrench of the robot, but rather its behavior [6]. In the field of robotics, these issues have been firstly addressed in some seminal works [7, 8, 9], which led to the widely used *impedance control* methodology. The port-based framework was an essential ingredient used in those works in order to formalize the proposed control methodology.

A general limitation of basic impedance control strategies is that to apply a specific desired interaction wrench, without feedback of the latter, a priori knowledge of the contact target's geometrical and mechanical properties is required. However, such knowledge is difficult to acquire in practice and, in fact, this contradicts the key advantage of impedance control to work in uncertain environments. A solution for the aforementioned drawback is to utilize information about the interaction wrench, either using force/torque measurements or model-based estimation, for modulating the stiffness of the impedance controller in order to regulate the interaction wrench to a desired value. However, the interaction wrench regulation comes at the cost of violating the passivity of the closed-loop system and, as a consequence, the contact stability is no longer guaranteed.

In this paper, we present an *energy-aware impedance control* approach for aerial physical interaction in the port-Hamiltonian framework. Our objective is to enhance the basic geometric impedance control approach with wrench regulation capabilities, while guaranteeing contact stability and safe interaction, using the concepts of energy tanks and energy routing. The intuitive idea of an energy-tank, first proposed in [10], is that it stores the energy dissipated by the control system and uses it to implement control actions that could violate the passivity of the closed-loop system, for instance the regulation of the interaction wrench in our case. On top of that, energy tanks allow the energy flow within the system to be observed and possibly used for high-level purposes, thus the controller becomes more *energy-aware* [5]

A unique feature of the presented port-Hamiltonian con-

troller is that it relies on the *control-by-interconnection* principle in which the control system is designed and treated as a virtual physical system connected to the actual physical robot via power-ports. Furthermore, the controller itself will be constructed as a network of energetic subsystems interconnected to each other in a power-preserving manner. The first advantage of this modular control-by-interconnection approach is that the designer can physically interpret the control system which in turn greatly simplifies the tuning process of its design parameters. Second, using the intuitive fact that two passive systems connected by a power-preserving interconnection is again a passive system, the stability analysis of the overall closed loop system can be divided into simpler passivity checks of each energetic subsystem [11]. In addition, these checks do not have to be repeated if extra modules are added.

The specific contributions of this paper are as follows:

- Formulate the impedance control problem of a fully-actuated MAV using the control-by-interconnection port-Hamiltonian approach.
- Represent all the system dynamics using the Lie-group approach which takes into account the underlying geometric structures and allows for compact mathematical expressions.
- Exploit bond graphs for graphical representation of the port-Hamiltonian models and show how it is a suitable tool for conducting passivity analysis just by inspection. Thus, eliminating the need for lengthy calculations encountered in analytical analysis of passivity.
- Augmenting the geometric impedance controller with the ability to regulate the interaction wrench with guaranteed contact stability with any conceivable passive environment using virtual energy tanks and energy routing.
- Develop a high-level algorithm that utilizes the energy and power observed within the virtual tank to guarantee safe interaction and detection of contact-loss situations.
- Validate the proposed control system in a campaign of simulations and experiments on a fully-actuated MAV.

The rest of this paper is outlined as follows: Sec. II contextualizes our work in the literature panorama compared to related state-of-the-art works. Sec. III presents the interpretation of an impedance controlled flying end-effector as the interconnection of several port-Hamiltonian subsystems. In Sec. IV, we present how the basic impedance controller can be augmented with wrench regulation capabilities by varying the stiffness of the controller and show how this comes at the cost of losing the passivity of the closed-loop system. Sec. V presents the details of the energy-aware impedance controller that allows the implementation of the wrench regulation without violating the passivity of the system. Sec. VI presents an extension to the energy-tank based controller that allows achieving a higher level of safety during interaction applications with potential contact-loss. We present extensive validation results of the proposed controller in Sec. VII, and discuss some key-aspects of our control methodology in Sec. VIII. Finally, we conclude in Sec. IX summarizing the contributions and outlining hints on future work.

II. RELATED WORKS

In this section, we present a number of related works in the aerial robotics and ground manipulators literature. For an introduction to the subject, the reader is referred to [12] for the topic of interaction using ground-based manipulators, to [13] for a review of fully-actuated multirotor vehicles, and to [2] for a review of interaction using aerial manipulators.

A. Interaction control of ground-manipulators

The basic geometric impedance controller underlying our work is based on the work of [14, 15], developed in the Lagrange formalism for rigid serial manipulators, and the work of [16], developed in the port-Hamiltonian formalism for robotic grasping applications. In our previous work [17], we have shown that the geometric impedance controller of [14, 15, 16] can be derived systematically using the energy-balancing passivity-based control (EB-PBC) technique for the class of flying end-effectors we are considering here.

In our current paper, we use the constant impedance controller of [17] as the baseline controller that is augmented with stiffness modulation and energy tanks for regulating the interaction wrench. First, in Sec. III, we reformulate this baseline controller as a network of several port-Hamiltonian subsystems interconnected together. We also show this network-interpretation and its bond graph representation allows proving the system's passivity, recovering the results of [17].

B. Energy-tanks augmentation

The use of energy tanks for interaction control of ground manipulators has increased in recent years. In most cases, they are employed to passivize an otherwise non-passive control system. In [18] an energy tank is used to ensure passivity after a signal-based control loop is added to the impedance controller for regulating the interaction force. In [19, 20] variable stiffness impedance control is used to deal with varying tissue stiffness during a surgical needle insertion task by a robotic manipulator, where it is shown how varying the stiffness would normally cause unstable behavior due to the loss of passivity.

There have been two different approaches in which energy-tanks have been implemented in the literature; a signal-based approach and a port-based approach. Examples of purely signal based implementations on the one hand can be found in [18] as well as a primitive version of our current work [21]. Although, from a theoretical point of view, this signal-based approach succeeds in restoring the closed-loop system's passivity, it prevents the full benefits of the port-based approach to be reaped, such as the intuitive and straightforward analysis of energy flows within the system.

Alternatively, the works of [22, 23] have shown how port-based implementations can be realized. In such an approach, that we adopt in our work, the energy tank is considered as a part of the virtual physical system connected through power ports and power-continuous structures. This guarantees power continuity, and forces the designer to explicitly consider the flow of energy within the system which is necessary to

conceptually understand the principles behind energy-tanks and their added value.

Next to passivity, energy tanks have also been used to implement high-level energy-aware control objectives. In order to achieve generally safe behavior of a robotic system in the vicinity of humans, [24, 23, 25] presented energy-tank-based approaches that limit the total energy in the system and the power injected into the robot by the controller. In contrast to the standard impedance controller used in [24, 23], our work focuses on the safety issues that arise when this interaction wrench is being regulated.

In [18] it is discussed how the application of significant interaction forces to the environment may lead to unsafe behavior even with passivity guaranteed, in case of an unexpected loss of contact with this environment. Thus, a solution to this safety problem is suggested in [18] based on a signal-based approach that compares the direction of the desired force "vector" and the relative displacement "vector" of the end-effector's position and the desired virtual position. In our work, we propose a different method for dealing with potential contact-loss when regulating the interaction wrench, detailed in Sec. VI. In short, our proposed approach detects contact loss by monitoring the energy that is drawn from the energy tank, and subsequently responding by altering the behavior of the energy tank. In contrast to the contact-loss stabilization technique of [18], our method monitors just one single state, i.e. the energy stored in the virtual tank, as opposed to a robot's position and orientation. Therefore, safety restrictions can be defined more abstractly for a wider variety of tasks and environments.

C. Interaction control of flying-manipulators

In the context of aerial robotics, several hybrid pose/wrench control methods have been proposed in the literature including [26, 4, 27]. However, as mentioned in Sec. I, such signal-based controllers are considered less suited for physical interaction due to their need for accurate models of the environment in order to guarantee contact stability.

Indirect force control techniques, such as impedance and admittance control, are more appropriate for interaction with unmodeled environments. [28] presented a variable impedance controller for aerial interaction of a quadrotor. A force regulator is implemented as an outer loop of the variable impedance controller. The external force is estimated by the position information and stiffness of the environment, which is assumed to be a linear spring. In [29], a physical-virtual impedance controller was implemented by incorporating a compliant robotic arm with a multi-rotor platform. In [1], an admittance controller with an external wrench observer was implemented on a fully-actuated hexarotor platform, similar to the platform we use in our work. Their approach relied on the geometric trajectory tracking controller introduced by [30], in which the controllers for the rotational and translational dynamics are designed separately.

In contrast to our proposed framework, the approach followed in [1] lacks consistency in respecting the geometric structure of the configuration space $SE(3)$. Controllers designed in this manner have been shown to be non-invariant

Table I: Nomenclature

Ψ_I, Ψ_B	Inertial and body-fixed reference frames
$\mathbf{H}_B^I \in SE(3)$	Relative pose of Ψ_B w.r.t. Ψ_I
$\mathbf{R}_B^I \in SO(3)$	Relative orientation of Ψ_B w.r.t. Ψ_I
$\boldsymbol{\xi}_B^I \in \mathbb{R}^3$	Position of the origin of Ψ_B expressed in Ψ_I
$\mathbf{T}_B^{B,I} \in \mathbb{R}^6$	Twist of Ψ_B (subscript) w.r.t. Ψ_I expressed in Ψ_B
$\boldsymbol{\omega}_B^{B,I} \in \mathbb{R}^3$	Angular velocity part of the twist $\mathbf{T}_B^{B,I}$
$\mathbf{v}_B^{B,I} \in \mathbb{R}^3$	Linear velocity part of the twist $\mathbf{T}_B^{B,I}$
$\tilde{\mathbf{T}}_B^{B,I} \in \mathfrak{se}(3)$	4×4 matrix representation of the twist $\mathbf{T}_B^{B,I}$
$\tilde{\mathbf{y}} \in \mathfrak{so}(3)$	3×3 skew-symmetric matrix representation of $\mathbf{y} \in \mathbb{R}^3$
$\mathbf{W}_{\text{src}}^B \in (\mathbb{R}^6)^*$	Wrench applied by the source (src) to the MAV expressed in Ψ_B
$\boldsymbol{\tau}_{\text{src}}^B \in (\mathbb{R}^3)^*$	Torque part of the wrench $\mathbf{W}_{\text{src}}^B$
$\mathbf{f}_{\text{src}}^B \in (\mathbb{R}^3)^*$	Force part of the wrench $\mathbf{W}_{\text{src}}^B$
$\mathbf{P}^B \in (\mathbb{R}^6)^*$	Generalized momentum of MAV expressed in Ψ_B
$\mathbf{P}_\omega \in (\mathbb{R}^3)^*$	Angular momentum part of \mathbf{P}^B
$\mathbf{P}_v \in (\mathbb{R}^3)^*$	Linear momentum part of \mathbf{P}^B
$\mathcal{I} \in \mathbb{R}^{6 \times 6}$	Generalized inertia tensor of MAV expressed in Ψ_B
$\mathbf{J} \in \mathbb{R}^{3 \times 3}$	Moment of inertia tensor of MAV expressed in Ψ_B
$m \in \mathbb{R}^+$	Mass of MAV

to coordinate changes [31]. Such geometric inconsistency could lead to many practical problems particularly for robots interacting with the environment [12].

In recent years there has been an increasing interest in port-Hamiltonian control approaches. The first use of port-based modeling and control concepts in the aerial robotics literature was in [32], where stabilization and tracking controllers were derived for generic underactuated vehicles and simulated for a ducted-fan UAV. Although the controllers were designed by standard passivity-based techniques, the presented approach included compensation of the MAV dynamics, non-passive projection, and added robustness by using integral action, which destroyed the passivity of the motion controller. In [33, 34], the authors used the interconnection and damping assignment PBC (IDA-PBC) approach for the decentralized control of a quadrotor/manipulator system. The approach was validated through some free-flight simulations.

III. CONTROL-BY-INTERCONNECTION INTERPRETATION

In this section, we will present the port-Hamiltonian formulation of the flying-end effector's dynamics augmented with a geometric constant impedance controller. In this representation, the impedance controller derived in [17] via EB-PBC will be reformulated in the control-by-interconnection approach by interpreting the controller as a network of energetic subsystems interconnected via power ports. First, we start by presenting the port-Hamiltonian equations of motion of the flying-end effector formulated using the Lie group approach using the special Euclidean group $SE(3)$ as its configuration space.

A. Flying-end Effector

In our work we consider the flying end-effector to be a fully-actuated MAV consisting of a single rigid body that is connected to a number of propellers via revolute joints actuated by electric motors. For control purposes, it is common to neglect the electric and mechanical dynamics of the MAV's

propellers, which is a valid assumption because they change at a faster time scale compared to the dynamics of the MAV's main body.

Let $\{\Psi_I : o_I, \hat{\mathbf{x}}_I, \hat{\mathbf{y}}_I, \hat{\mathbf{z}}_I\}$ denote a right-handed orthonormal inertial frame and $\{\Psi_B : o_B, \hat{\mathbf{x}}_B, \hat{\mathbf{y}}_B, \hat{\mathbf{z}}_B\}$ denote the body-fixed frame attached at an arbitrary orientation to the center of mass of the MAV's body. The state of the MAV is defined by the pair $(\mathbf{H}_B^I, \mathbf{P}^B)$ where $\mathbf{H}_B^I \in SE(3)$ denotes the relative pose of Ψ_B with respect to Ψ_I and $\mathbf{P}^B \in (\mathbb{R}^6)^*$ denotes the generalized momentum¹ of the MAV expressed in Ψ_B . We have that $\mathbf{P}^B := \mathcal{I}\mathbf{T}_B^{B,I}$ with $\mathcal{I} \in \mathbb{R}^{6 \times 6}$ denoting the generalized inertia tensor of the body and $\mathbf{T}_B^{B,I} \in \mathbb{R}^6$ denoting the body's twist (i.e. generalized velocity).

The equations of motion of the flying end-effector are then given by the *Euler-Poincare* equations [35, 36]:

$$\dot{\mathbf{H}}_B^I = \mathbf{H}_B^I \tilde{\mathbf{T}}_B^{B,I}, \quad (1)$$

$$\dot{\mathbf{P}}^B = \mathbf{J}_k(\mathbf{P}^B) \mathcal{I}^{-1} \mathbf{P}^B + \mathbf{W}_g^B + \mathbf{W}_c^B + \mathbf{W}_{\text{int}}^B, \quad (2)$$

where $\mathbf{W}_g^B, \mathbf{W}_c^B, \mathbf{W}_{\text{int}}^B \in (\mathbb{R}^6)^*$ denote the wrench applied to the MAV due to gravity, controlled propellers, and interaction with the environment, respectively. Further, the skew-symmetric matrix $\mathbf{J}_k(\mathbf{P}^B) \in \mathbb{R}^{6 \times 6}$ is defined as

$$\mathbf{J}_k(\mathbf{P}^B) := \begin{pmatrix} \tilde{\mathbf{P}}_\omega & \tilde{\mathbf{P}}_v \\ \tilde{\mathbf{P}}_v & \mathbf{0} \end{pmatrix}, \quad \mathbf{P}^B = \begin{pmatrix} \mathbf{P}_\omega \\ \mathbf{P}_v \end{pmatrix} \in (\mathbb{R}^6)^*, \quad (3)$$

whereas a summary of all notations in (1-3) can be found in Table I.

In terms of the individual rotational and translational components of the physical quantities mentioned above, the Euler-Poincare equations (1-3) are equivalent to the more common dynamic equations:

$$\dot{\mathbf{R}}_B^I = \mathbf{R}_B^I \tilde{\boldsymbol{\omega}}_B^{B,I}, \quad (4)$$

$$\dot{\boldsymbol{\xi}}_B^I = \mathbf{R}_B^I \tilde{\mathbf{v}}_B^{B,I}, \quad (5)$$

$$\mathbf{J} \dot{\boldsymbol{\omega}}_B^{B,I} = -\tilde{\boldsymbol{\omega}}_B^{B,I} \mathbf{J} \boldsymbol{\omega}_B^{B,I} + \boldsymbol{\tau}_c^B + \boldsymbol{\tau}_{\text{int}}^B, \quad (6)$$

$$m \dot{\mathbf{v}}_B^{B,I} = -m \tilde{\boldsymbol{\omega}}_B^{B,I} \mathbf{v}_B^{B,I} + \mathbf{f}_g^B + \mathbf{f}_c^B + \mathbf{f}_{\text{int}}^B, \quad (7)$$

where all symbols are defined in Table I.

The MAV's equations of motion (1-3) can be reformulated in the port-Hamiltonian framework as the explicit dynamical system [6, 37]:

$$\dot{\mathbf{H}}_B^I = \chi_{\mathbf{H}_B^I} (\partial_{\mathbf{P}^B} \mathcal{H}), \quad (8)$$

$$\dot{\mathbf{P}}^B = -\chi_{\mathbf{H}_B^I}^* (\partial_{\mathbf{H}_B^I} \mathcal{H}) + \mathbf{J}_k(\mathbf{P}^B) \partial_{\mathbf{P}^B} \mathcal{H} + \mathbf{W}_c^B + \mathbf{W}_{\text{int}}^B, \quad (9)$$

where the Hamiltonian $\mathcal{H}(\mathbf{x})$ is given by the sum of kinetic and gravitational potential energy of the MAV, i.e.

$$\begin{aligned} \mathcal{H}(\mathbf{x}) &= \mathcal{H}_k(\mathbf{P}^B) + \mathcal{H}_g(\mathbf{H}_B^I) \\ &= \frac{1}{2} (\mathbf{P}^B)^\top \mathcal{I}^{-1} \mathbf{P}^B + m (\boldsymbol{\xi}_B^I)^\top \mathbf{g}, \end{aligned} \quad (10)$$

with $\mathbf{g} \in \mathbb{R}^3$ denoting (minus) the direction of the gravitational acceleration in the inertial frame Ψ_I . We

¹Although $(\mathbb{R}^n)^* \cong \mathbb{R}^n$ for all n , we denote in our work the space of generalized momenta and wrenches by $(\mathbb{R}^6)^*$ to stress their covector nature which is crucial to consider when changing coordinates later.

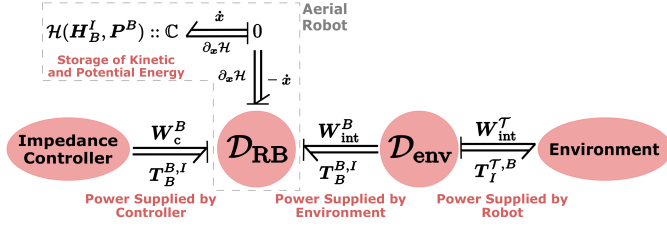


Figure 1: Port-based representation of the aerial robot's port-Hamiltonian model connected to its controller and the environment via power ports characterizing the energy exchange between them.

denote by $\partial_{P^B}\mathcal{H}$ and $\partial_{H_B^I}\mathcal{H}$ the partial differentiation of the function \mathcal{H} with respect to P^B and H_B^I , respectively. We also have that $\partial_{P^B}\mathcal{H} = \mathcal{I}^{-1}P^B = T_{B^I}^{B,I}$. The map $\chi_{H_B^I} : \mathbb{R}^6 \rightarrow T_{H_B^I}SE(3)$ is defined such that (8) and (1) are equivalent, whereas $\chi_{H_B^I}^* : T_{H_B^I}^*SE(3) \rightarrow (\mathbb{R}^6)^*$ is the dual map of $\chi_{H_B^I}$.

Remark 1: The first term on the right-hand side of (9) corresponds to the gravity wrench W_g^B in (2), which simply represents the wrench due to gravity as *minus the gradient of a potential function*. Such formulation will be also used later for representing the wrench due to a geometric six-dimensional spring. The reader is referred to [37, Ch.4] for the procedure of evaluating $\chi_{H_B^I}^*$.

The explicit port-Hamiltonian system (8-9) can be also represented in an implicit form as depicted in Fig. 1 showing the aerial robot's model as an open dynamical system interacting with its controller and the environment via power ports. The aerial robot's implicit port-Hamiltonian model consists of *i)* an energy storage \mathbb{C} -element that characterizes the kinetic energy and gravitational potential energy of the robot, and *ii)* a Dirac structure \mathcal{D}_{RB} that characterizes the exchange of energy between the robot and the external world including the impedance controller and the environment.

With reference to Fig. 1, the energy storage element has a state variable $x := (H_B^I, P^B) \in SE(3) \times (\mathbb{R}^6)^*$ and its corresponding flow and effort variables are given, respectively, by

$$\begin{aligned} \dot{x} &= \begin{pmatrix} \dot{H}_B^I \\ \dot{P}^B \end{pmatrix} \in T_{H_B^I}SE(3) \times (\mathbb{R}^6)^*, \\ \partial_x \mathcal{H} &= \begin{pmatrix} \partial_{H_B^I} \mathcal{H} \\ \partial_{P^B} \mathcal{H} \end{pmatrix} \in T_{H_B^I}^*SE(3) \times \mathbb{R}^6. \end{aligned}$$

The Dirac structure \mathcal{D}_{RB} is defined as the relation corresponding to the skew-symmetric map

$$\begin{pmatrix} -\dot{H}_B^I \\ -\dot{P}^B \\ T_{B^I}^{B,I} \\ T_{B^I}^{B,I} \end{pmatrix} = \begin{pmatrix} \mathbf{0} & -\chi_{H_B^I} & \mathbf{0} & \mathbf{0} \\ \chi_{H_B^I}^* & -J_k(P^B) & -I_6 & -I_6 \\ \mathbf{0} & I_6 & \mathbf{0} & \mathbf{0} \\ \mathbf{0} & I_6 & \mathbf{0} & \mathbf{0} \end{pmatrix} \begin{pmatrix} \partial_{H_B^I} \mathcal{H} \\ \partial_{P^B} \mathcal{H} \\ W_c^B \\ W_{int}^B \end{pmatrix}. \quad (11)$$

The Dirac structure \mathcal{D}_{RB} encodes the energy balance given by

$$\dot{\mathcal{H}}_g + \dot{\mathcal{H}}_k = (W_c^B)^\top T_{B^I}^{B,I} + (W_{int}^B)^\top T_{B^I}^{B,I}, \quad (12)$$

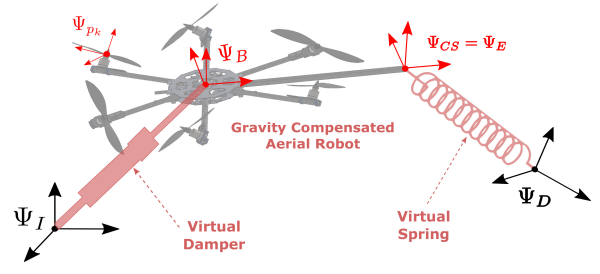


Figure 2: Control-by-interconnection interpretation of the impedance controller as a virtual spring and a virtual damper attached to the aerial robot with gravity-compensation.

which simply states that the rate of change in the total energy $\mathcal{H} = \mathcal{H}_g + \mathcal{H}_k$ stored by the MAV along solutions of the dynamical system represented in (11) is equal to the power supplied by the controller and the environment, as illustrated in the bond graph of Fig. 1.

It is useful to describe the interaction between the robot and the environment in a frame Ψ_τ fixed to the target to be physically contacted by the aerial robot. The robot's body twist $T_{B^I}^{B,I}$ and the interaction wrench applied to the robot W_{int}^B are related to their counterparts in the target frame Ψ_τ by the skew-symmetric map

$$\begin{pmatrix} W_{int}^B \\ T_I^{T,B} \end{pmatrix} = \begin{pmatrix} \mathbf{0} & Ad_{H_B^I}^\top \\ -Ad_{H_B^I} & \mathbf{0} \end{pmatrix} \begin{pmatrix} T_{B^I}^{B,I} \\ W_{int}^T \end{pmatrix}, \quad (13)$$

where for any $H \in SE(3)$ the matrix $Ad_H \in \mathbb{R}^{6 \times 6}$ corresponds to the adjoint map of the Lie group $SE(3)$ and is defined by

$$Ad_H = \begin{pmatrix} R & \mathbf{0} \\ \tilde{\xi}R & R \end{pmatrix}, \quad H = \begin{pmatrix} R & \xi \\ \mathbf{0} & 1 \end{pmatrix}. \quad (14)$$

Note that the difference in transforming coordinates of twists compared to wrenches is due to their different tensorial natures. The Dirac structure \mathcal{D}_{env} , given by the relation corresponding to the map (13), states that the power supplied by the environment to the aerial robot is equivalent to *minus* the power supplied by the robot to the environment, i.e.

$$(W_{int}^B)^\top T_{B^I}^{B,I} = -(W_{int}^T)^\top T_I^{T,B}. \quad (15)$$

B. Impedance Controller

Now we turn attention to the control-by-interconnection interpretation of the constant impedance controller derived in [17] which serves as the basic module within our proposed control system detailed in Sec. V. With reference to Fig. 2, the impedance controller of [17] emulates a virtual spring and a virtual damper attached to the aerial robot with the gravity being compensated by the controller. The virtual spring is connected between the center of stiffness frame Ψ_{CS} (placed at the robot's end effector frame Ψ_E) and the desired frame Ψ_D . Whereas, the virtual damper is connected between the robot's body frame Ψ_B and the inertial frame Ψ_I for asymptotically stabilizing the system.

1) *Virtual spring*: A virtual spring with constant stiffness is represented in the port-Hamiltonian framework by the combination of an energy storage element and a transformation, as shown in Fig. 3. The energy storage element, denoted by \mathbb{C} , is characterized by the state variable $\mathbf{H}_{CS}^D \in SE(3)$ and the elastic potential energy Hamiltonian $\mathcal{H}_p : SE(3) \rightarrow \mathbb{R}$ given by

$$\begin{aligned} \mathcal{H}_p(\mathbf{H}_{CS}^D) = & -\text{tr}(\mathbf{G}_o(\mathbf{R}_{CS}^D - \mathbf{I}_3)) + \frac{1}{4}(\boldsymbol{\xi}_{CS}^D)^\top \mathbf{K}_t \boldsymbol{\xi}_{CS}^D \\ & + \frac{1}{4}(\boldsymbol{\xi}_{CS}^D)^\top \mathbf{R}_{CS}^D \mathbf{K}_t (\mathbf{R}_{CS}^D)^\top \boldsymbol{\xi}_{CS}^D, \end{aligned} \quad (16)$$

where $\mathbf{K}_t \in \mathbb{R}^{3 \times 3}$ is the constant translation stiffness matrix, $\mathbf{G}_o \in \mathbb{R}^{3 \times 3}$ is the constant orientation co-stiffness matrix, and $\mathbf{R}_{CS}^D \in SO(3)$ and $\boldsymbol{\xi}_{CS}^D \in \mathbb{R}^3$ are the rotation and translation components of $\mathbf{H}_{CS}^D \in SE(3)$. The flow and effort variables of the storage element are given respectively by $\dot{\mathbf{H}}_{CS}^D \in T_{\mathbf{H}_{CS}^D} SE(3)$ and $\partial_{\mathbf{H}_{CS}^D} \mathcal{H}_p \in T_{\mathbf{H}_{CS}^D}^* SE(3)$, with their dual product corresponding to the rate of change of energy stored, i.e.

$$\dot{\mathcal{H}}_p = \left\langle \partial_{\mathbf{H}_{CS}^D} \mathcal{H}_p \middle| \dot{\mathbf{H}}_{CS}^D \right\rangle_{SE}. \quad (17)$$

The modulated transformer MTF implements the map

$$\begin{pmatrix} \dot{\mathbf{H}}_{CS}^D \\ \mathbf{W}_{\text{spr}}^{CS} \end{pmatrix} = \begin{pmatrix} \mathbf{0} & \chi_{\mathbf{H}_{CS}^D} \\ \chi_{\mathbf{H}_{CS}^D}^* & \mathbf{0} \end{pmatrix} \begin{pmatrix} \partial_{\mathbf{H}_{CS}^D} \mathcal{H}_p \\ \mathbf{T}_{CS}^{CS,D} \end{pmatrix}, \quad (18)$$

where the first equation corresponds to the kinematics relation between $\dot{\mathbf{H}}_{CS}^D$ and $\mathbf{T}_{CS}^{CS,D} \in \mathbb{R}^6$ which is the relative twist between the two ends of the spring (i.e. Ψ_{CS} and Ψ_D). The second equation in (18) relates the differential of the potential function (16) to $\mathbf{W}_{\text{spr}}^{CS} \in (\mathbb{R}^6)^*$ which corresponds to the wrench applied to the spring by the body it is attached to at Ψ_{CS} (i.e. the aerial robot). The exact expression of the wrench is given by [17]:

$$\mathbf{W}_{\text{spr}}^{CS} = \begin{pmatrix} \boldsymbol{\tau}_{\text{spr}}^{CS} \\ \mathbf{f}_{\text{spr}}^{CS} \end{pmatrix}, \quad (19)$$

$$\boldsymbol{\tau}_{\text{spr}}^{CS} = 2\text{sk}(\mathbf{G}_o \mathbf{R}_{CS}^D) + \text{sk}(\mathbf{G}_t \mathbf{R}_D^{CS} \tilde{\boldsymbol{\xi}}_{CS}^D \tilde{\boldsymbol{\xi}}_{CS}^D \mathbf{R}_{CS}^D), \quad (20)$$

$$\mathbf{f}_{\text{spr}}^{CS} = \mathbf{R}_D^{CS} \text{sk}(\mathbf{G}_t \tilde{\boldsymbol{\xi}}_{CS}^D) \mathbf{R}_{CS}^D + \text{sk}(\mathbf{G}_t \mathbf{R}_D^{CS} \tilde{\boldsymbol{\xi}}_{CS}^D \mathbf{R}_{CS}^D). \quad (21)$$

where $\text{sk}(A)$ denotes the skew-symmetric part of the matrix $A \in \mathbb{R}^{3 \times 3}$, $\mathbf{G}_t \in \mathbb{R}^{3 \times 3}$ is the translation co-stiffness matrix corresponding to \mathbf{K}_t , and $\boldsymbol{\tau}_{\text{spr}}^{CS}, \mathbf{f}_{\text{spr}}^{CS} \in \mathfrak{so}^*(3)$ are the skew-symmetric matrix counterparts of the covectors $\boldsymbol{\tau}_{\text{spr}}^{CS}, \mathbf{f}_{\text{spr}}^{CS} \in (\mathbb{R}^3)^*$.

Using (18), one can rewrite the energy balance (17) as

$$\begin{aligned} \dot{\mathcal{H}}_p &= \left\langle \partial_{\mathbf{H}_{CS}^D} \mathcal{H}_p \middle| \chi_{\mathbf{H}_{CS}^D}(\mathbf{T}_{CS}^{CS,D}) \right\rangle_{SE} \\ &= \left\langle \chi_{\mathbf{H}_{CS}^D}^* (\partial_{\mathbf{H}_{CS}^D} \mathcal{H}_p) \middle| \mathbf{T}_{CS}^{CS,D} \right\rangle_{\mathbb{R}^6} = (\mathbf{W}_{\text{spr}}^{CS})^\top \mathbf{T}_{CS}^{CS,D}. \end{aligned} \quad (22)$$

2) *Gravity compensation*: Similar to the virtual spring, the gravity compensation is also represented by a combination of an energy storage element and a transformation, as shown in Fig. 3. The storage element is characterized by the state $\mathbf{H}_B^I \in SE(3)$ and minus the gravitational potential energy Hamiltonian $-\mathcal{H}_g : SE(3) \rightarrow \mathbb{R}$ given by

$$-\mathcal{H}_g(\mathbf{H}_B^I) = -m(\boldsymbol{\xi}_B^I)^\top \mathbf{g}. \quad (23)$$

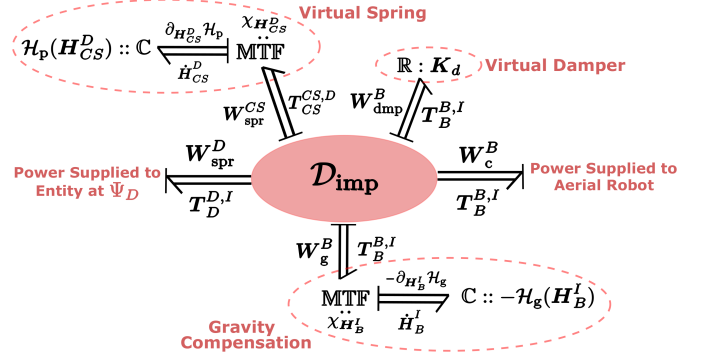


Figure 3: Port-based representation of the impedance controller as a number of energetic subsystems.

The rate of change of the stored energy is given by

$$-\dot{\mathcal{H}}_g = \left\langle -\partial_{\mathbf{H}_B^I} \mathcal{H}_g \middle| \dot{\mathbf{H}}_B^I \right\rangle_{SE}, \quad (24)$$

where $\dot{\mathbf{H}}_B^I \in T_{\mathbf{H}_B^I} SE(3)$ and $-\partial_{\mathbf{H}_B^I} \mathcal{H}_g \in T_{\mathbf{H}_B^I}^* SE(3)$ are the flow and effort variables of the energy storage element, respectively.

The modulated transformer associated to the storage element implements the map

$$\begin{pmatrix} \dot{\mathbf{H}}_B^I \\ \mathbf{W}_g^B \end{pmatrix} = \begin{pmatrix} \mathbf{0} & \chi_{\mathbf{H}_B^I} \\ \chi_{\mathbf{H}_B^I}^* & \mathbf{0} \end{pmatrix} \begin{pmatrix} -\partial_{\mathbf{H}_B^I} \mathcal{H}_g \\ \mathbf{T}_B^{B,I} \end{pmatrix}, \quad (25)$$

where the first equation is a kinematics relation and the second corresponds to the wrench $\mathbf{W}_g^B \in (\mathbb{R}^6)^*$ applied to the aerial robot due to gravity, and $\mathbf{T}_B^{B,I} \in \mathbb{R}^6$ is the robot's body twist.

Similar to (22), one can rewrite the energy balance (24) as

$$-\dot{\mathcal{H}}_g = (\mathbf{W}_g^B)^\top \mathbf{T}_B^{B,I}. \quad (26)$$

3) *Virtual damper*: The virtual damper is represented in the bond graph of Fig. 3 by an energy dissipation element, denoted by \mathbb{R} , which is characterized by the static relation between its flow $\mathbf{T}_B^{B,I} \in \mathbb{R}^6$ and effort $\mathbf{W}_{\text{dmp}}^B \in (\mathbb{R}^6)^*$ defined as

$$\mathbf{W}_{\text{dmp}}^B = \mathbf{K}_d \mathbf{T}_B^{B,I}, \quad (27)$$

where $\mathbf{K}_d \in \mathbb{R}^{6 \times 6}$ is a symmetric positive semi-definite matrix. This static relation implies that power always flows towards the dissipation element, i.e.

$$\langle \mathbf{W}_{\text{dmp}}^B \middle| \mathbf{T}_B^{B,I} \rangle_{\mathbb{R}^6} = (\mathbf{T}_B^{B,I})^\top \mathbf{K}_d \mathbf{T}_B^{B,I} \geq 0, \quad (28)$$

which represents the “free energy” dissipated by the controller emulating a virtual damper.

4) *External power ports*: The impedance controller depicted in Fig. 3 has two power ports that are open for interconnection to external systems. The first port $(\mathbf{W}_c^B, \mathbf{T}_B^{B,I})$ characterizes the power supplied to the aerial robot for control. The causality of this port is such that the body twist $\mathbf{T}_B^{B,I}$ is directed from the aerial robot to the impedance controller, whereas the control wrench \mathbf{W}_c^B is directed from the impedance controller to the aerial robot.

The second port $(\mathbf{W}_{\text{spr}}^D, \mathbf{T}_D^{D,I})$ characterizes the power flowing between the impedance controller and the entity connected to the virtual desired frame Ψ_D . This entity should provide

the twist of Ψ_D with respect to Ψ_I as an input to the impedance controller, which in our case is a trajectory or set-point generation algorithm. However, it is important to note that changing the desired virtual set-point affects the energy stored of the controller as a dynamical system. This can be clearly seen in Fig. 2 since Ψ_D corresponds to one end of the virtual spring. Thus, changing the virtual set-point will affect the passivity of the closed-loop system, as will be discussed later.

5) *Dirac structure*: Central to the control-by-interconnection interpretation of the impedance controller in Fig. 3 is the Dirac structure \mathcal{D}_{imp} given by the relation corresponding to the skew-symmetric map

$$\begin{pmatrix} \mathbf{T}_{CS}^{CS,D} \\ \mathbf{T}_B^{B,I} \\ \mathbf{T}_B^{B,I} \\ \mathbf{W}_{\text{spr}}^D \\ \mathbf{W}_c^B \end{pmatrix} = \mathcal{J}_{\text{imp}} \begin{pmatrix} \mathbf{W}_{\text{spr}}^{CS} \\ \mathbf{W}_g^B \\ \mathbf{W}_{\text{dmp}}^B \\ \mathbf{T}_D^{D,I} \\ \mathbf{T}_B^{B,I} \end{pmatrix}, \quad (29)$$

$$\mathcal{J}_{\text{imp}} := \begin{pmatrix} 0 & 0 & 0 & -\text{Ad}_{\mathbf{H}_D^{CS}} & \text{Ad}_{\mathbf{H}_B^{CS}} \\ 0 & 0 & 0 & 0 & \mathbf{I}_6 \\ 0 & 0 & 0 & 0 & \mathbf{I}_6 \\ \text{Ad}_{\mathbf{H}_D^{CS}}^\top & 0 & 0 & 0 & 0 \\ -\text{Ad}_{\mathbf{H}_B^{CS}}^\top & -\mathbf{I}_6 & -\mathbf{I}_6 & 0 & 0 \end{pmatrix}.$$

The first equation in (29) corresponds to the twist relation

$$\begin{aligned} \mathbf{T}_{CS}^{CS,D} &= \text{Ad}_{\mathbf{H}_B^{CS}} \mathbf{T}_B^{B,I} - \text{Ad}_{\mathbf{H}_D^{CS}} \mathbf{T}_D^{D,I} \\ &= \mathbf{T}_B^{CS,I} - \mathbf{T}_D^{CS,I} = \mathbf{T}_B^{CS,D}, \end{aligned}$$

which is true since Ψ_B and Ψ_{CS} are both attached to the same body. The fourth equation corresponds to the change of coordinates of the spring wrench from Ψ_{CS} to Ψ_D . Finally, the last equation corresponds to the impedance control law

$$\mathbf{W}_c^B = -\text{Ad}_{\mathbf{H}_B^{CS}}^\top \mathbf{W}_{\text{spr}}^{CS} - \mathbf{W}_g^B - \mathbf{W}_{\text{dmp}}^B, \quad (30)$$

which is equivalent to the EB-PBC law of [17].

It is straightforward to check that the Dirac structure \mathcal{D}_{imp} corresponding to (29) encodes the power balance given by

$$\begin{aligned} (\mathbf{W}_{\text{spr}}^{CS})^\top \mathbf{T}_{CS}^{CS,D} + (\mathbf{W}_g^B)^\top \mathbf{T}_B^{B,I} + (\mathbf{W}_{\text{dmp}}^B)^\top \mathbf{T}_B^{B,I} \\ + (\mathbf{W}_{\text{spr}}^D)^\top \mathbf{T}_D^{D,I} + (\mathbf{W}_c^B)^\top \mathbf{T}_B^{B,I} = 0. \end{aligned} \quad (31)$$

Therefore, the power supplied by the controller $(\mathbf{W}_c^B)^\top \mathbf{T}_B^{B,I}$ can be expressed, using (22, 26, 28), as

$$(\mathbf{W}_c^B)^\top \mathbf{T}_B^{B,I} = -\dot{\mathcal{H}}_p + \dot{\mathcal{H}}_g - (\mathbf{T}_B^{B,I})^\top \mathbf{K}_d \mathbf{T}_B^{B,I} - (\mathbf{W}_{\text{spr}}^D)^\top \mathbf{T}_D^{D,I}. \quad (32)$$

In conclusion, the network of interconnected elements depicted in Fig. 3 is the control by interconnection interpretation of the impedance controller derived by EB-PBC in [17]. This controller emulates a virtual spring and virtual damper attached to the gravity-compensated aerial robot.

C. Passivity Analysis of Closed-loop System

Now we turn attention to analyzing the passivity of the closed-loop system, that includes the aerial robot and the impedance controller, with respect to the interaction port $(\mathbf{W}_{\text{int}}^B, \mathbf{T}_B^{B,I})$ characterizing the power supplied by the environment, as shown in Fig. 4. Intuitively speaking, a passive system is a system that can only dissipate or store energy, thus its total stored power is always non-increasing.

In the context of physical interaction, guaranteeing passivity of the closed-loop system is an effective way to ensure stable physical contact with an unknown passive environment without assuming a specific structure or model for it. In fact, it has been shown in [5] that for any non-passive closed-loop system, one can always construct a passive environment that results in unstable behavior during interaction.

Thanks to the port-Hamiltonian formulation of the overall system presented above, the passivity analysis is easily performed by combining the energy balances of the Dirac structures shown in Fig. 4. By substituting the power supplied by the controller (32) in the aerial robot's energy balance (12), one has that

$$\begin{aligned} \dot{\mathcal{H}}_g + \dot{\mathcal{H}}_k &= -\dot{\mathcal{H}}_p + \dot{\mathcal{H}}_g - (\mathbf{T}_B^{B,I})^\top \mathbf{K}_d \mathbf{T}_B^{B,I} \\ &\quad - (\mathbf{W}_{\text{spr}}^D)^\top \mathbf{T}_D^{D,I} + (\mathbf{W}_{\text{int}}^B)^\top \mathbf{T}_B^{B,I}, \end{aligned}$$

which can be rewritten as

$$\dot{\mathcal{H}}_k + \dot{\mathcal{H}}_p = -(\mathbf{T}_B^{B,I})^\top \mathbf{K}_d \mathbf{T}_B^{B,I} - (\mathbf{W}_{\text{spr}}^D)^\top \mathbf{T}_D^{D,I} + (\mathbf{W}_{\text{int}}^B)^\top \mathbf{T}_B^{B,I}, \quad (33)$$

under the assumption that the gravitational energy of the aerial robot has been perfectly compensated by the controller.

Now we take a closer look at the energy balance (33) to assess passivity. The left-hand-side of (33) corresponds to the rate of change of the total energy stored by the closed-loop system. On the other hand, the right-hand-side consists of the sum of the power dissipated by the virtual damper, the power due to changing the virtual spring's end connected to Ψ_D , and the power exchanged with the environment during interaction.

First, the power dissipated by the virtual damper $(\mathbf{T}_B^{B,I})^\top \mathbf{K}_d \mathbf{T}_B^{B,I}$ is always non-negative and thus contributes positively to the passivity of the system. As for the power due to changing Ψ_D , by the subsystem named *virtual set-point* in Fig. 4, its power is indefinite. Thus, it is a non-passive action that could inject energy into the virtual spring. However, under the assumption that Ψ_D changes during interaction in a piecewise constant or quasi-static manner such that

$$-(\mathbf{W}_{\text{spr}}^D)^\top \mathbf{T}_D^{D,I} < (\mathbf{T}_B^{B,I})^\top \mathbf{K}_d \mathbf{T}_B^{B,I}, \quad (34)$$

then changing the virtual set-point does not violate the passivity.

Another factor that could potentially violate the passivity of the closed-loop system is imperfect gravity compensation. In that case, the right-hand side of (33) would have an extra sign-indefinite term given by $(\delta \mathbf{W}_g^B)^\top \mathbf{T}_B^{B,I}$ where $\delta \mathbf{W}_g^B \in (\mathbb{R}^6)^*$ corresponds to the error in estimating the gravitational wrench applied on the aerial robot. However, from (23) it can be seen that this error depends on the parametric uncertainty of the robot's mass and gravitational acceleration which in

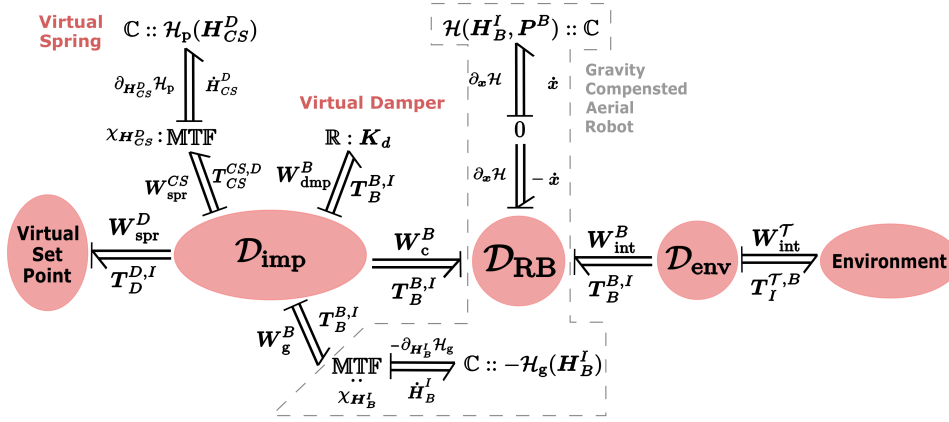


Figure 4: Port-based representation of the closed-loop system consisting of the impedance controller, the aerial robot, and the environment.

practice could be easily identified empirically. Therefore, the power injected due to imperfect gravity compensation could be assumed to be negligible compared to the power dissipated by the virtual damper. In fact, this should also be assumed for other uncertainties such as modeling errors and communication delays.

To summarize, under the aforementioned assumptions, we can express the energy balance (33) as

$$\dot{\mathcal{H}}_k + \dot{\mathcal{H}}_p \leq (\mathbf{W}_{int}^B)^\top \mathbf{T}_B^{B,I}, \quad (35)$$

which ensures the closed-loop system's passivity with respect to the interaction port $(\mathbf{W}_{int}^B, \mathbf{T}_B^{B,I})$. Thus, contact stability of the impedance-controlled aerial robot interacting with any conceivable passive environment is guaranteed.

It is important to note the simplicity of conducting the passivity analysis using the port-Hamiltonian formulation presented which naturally explicates the topology of energy flow within the system. Such straightforward analytical analysis could be simplified even further using the bond graph in Fig. 4 which allows checking the passivity by graphical inspection. We will demonstrate such procedure in Sec. V-D when the complete energy-aware controller is presented.

IV. INTERACTION WRENCH REGULATION

The basic impedance controller presented above does not allow regulating the interaction wrench with the environment to a desired value. In practice, such missing feature is certainly a prerequisite for high-precision interaction tasks.

In this section, we show how the interaction wrench can be regulated by modulating the stiffness of an additional virtual spring. Thus, the proposed impedance controller will comprise of two virtual springs, one with constant stiffness and another with variable stiffness, as shown in Fig. 5.

The choice of adding a new virtual spring with modulated stiffness has the advantage of *separation of concerns*. On one hand, the constant stiffness spring can be tuned for optimized motion control as well as shaping the general impedance behavior of the robot, for instance when establishing initial contact. On the other hand, the variable stiffness can be designed focusing on the goal of wrench regulation which will be shown to be a passivity-violating action.

Next, we present the details of the variable-stiffness controller starting by the wrench observer used to estimate the interaction wrench between the aerial robot and the environment.

A. Interaction Wrench Observer

Consider the momentum dynamics of the aerial robot given by the second equation in (11), which can be rewritten as

$$\dot{\mathbf{P}}^B = \underbrace{\mathbf{J}_k(\mathbf{P}^B) \mathcal{I}^{-1} \mathbf{P}^B + \mathbf{W}_g^B + \mathbf{W}_c^B + \mathbf{W}_{int}^B}_{=: \mathbf{f}(\mathbf{P}^B, \mathbf{W}_c^B)}, \quad (36)$$

which includes the interaction wrench \mathbf{W}_{int}^B applied to the aerial robot that we wish to estimate.

Similar to [38, 39, 40, 41], a wrench observer that provides an estimate $\hat{\mathbf{W}}_{int}^B \in (\mathbb{R}^6)^*$ of the interaction wrench applied to the aerial robot has the form

$$\hat{\mathbf{W}}_{int}^B = \mathbf{K}_o(\mathbf{P}^B - \hat{\mathbf{P}}), \quad (37)$$

$$\dot{\hat{\mathbf{W}}}_{int}^B = \mathbf{f}(\mathbf{P}^B, \mathbf{W}_c^B) + \mathbf{K}_o(\mathbf{P}^B - \hat{\mathbf{P}}), \quad (38)$$

where $\hat{\mathbf{P}} \in \mathbb{R}^6$ is an estimate of the actual body momentum, and $\mathbf{K}_o \in \mathbb{R}^{6 \times 6}$ is a positive diagonal matrix of observer gains.

The relation between the actual interaction wrench \mathbf{W}_{int}^B and the estimated one $\hat{\mathbf{W}}_{int}^B$ can be derived by substituting (36, 38) into the time derivative of (37) which yields

$$\dot{\hat{\mathbf{W}}}_{int}^B + \mathbf{K}_o \hat{\mathbf{W}}_{int}^B = \mathbf{K}_o \mathbf{W}_{int}^B, \quad (39)$$

which represents six first-order filters for each component of the interaction wrench, since \mathbf{K}_o is a diagonal matrix by construction.

In practice, the actual momentum dynamics (36) includes other external wrenches e.g. aerodynamic disturbances, unmodeled dynamics, and parametric uncertainties. The wrench computed from the observer (37,38) will actually be an estimate of all the external disturbances of the system and not just the interaction wrench.

The energy-aware control scheme we present in this work is independent of the wrench estimation/measurement technique used. Therefore, the basic wrench observer (37,38) could be

The spring wrench corresponding to (45) will consequently contain extra terms compared to (19) which can be shown to be equal to [6]

$$\mathbf{W}_{\text{spr},v}^{CS} = \begin{pmatrix} \boldsymbol{\tau}_{\text{spr},v}^{CS} \\ \mathbf{f}_{\text{spr},v}^{CS} \end{pmatrix}, \quad (46)$$

$$\begin{aligned} \tilde{\boldsymbol{\tau}}_{\text{spr},v}^{CS} &= 2\text{sk}(\bar{\mathbf{G}}_o \mathbf{R}_{CS}^D) + \text{sk}(\bar{\mathbf{G}}_t \mathbf{R}_D^{CS} \tilde{\boldsymbol{\xi}}_{CS}^D \tilde{\boldsymbol{\xi}}_{CS}^D \mathbf{R}_{CS}^D) \\ &\quad + 2\text{sk}(\bar{\mathbf{G}}_c \tilde{\boldsymbol{\xi}}_{CS}^D \mathbf{R}_{CS}^D), \end{aligned} \quad (47)$$

$$\begin{aligned} \tilde{\mathbf{f}}_{\text{spr},v}^{CS} &= \mathbf{R}_D^{CS} \text{sk}(\bar{\mathbf{G}}_t \tilde{\boldsymbol{\xi}}_{CS}^D) \mathbf{R}_{CS}^D + \text{sk}(\bar{\mathbf{G}}_t \mathbf{R}_D^{CS} \tilde{\boldsymbol{\xi}}_{CS}^D \mathbf{R}_{CS}^D) \\ &\quad + 2\text{sk}(\bar{\mathbf{G}}_c \mathbf{R}_{CS}^D), \end{aligned} \quad (48)$$

where $\bar{\mathbf{G}}_t \in \mathbb{R}^{3 \times 3}$ is the translation co-stiffness matrix corresponding to $\bar{\mathbf{K}}_t$.

The potential function of the variable-stiffness spring $\mathcal{H}_{p,v}$ satisfies the energy balance

$$\dot{\mathcal{H}}_{p,v} = \langle \mathbf{W}_{\text{spr},v}^{CS} | \mathbf{T}_{CS}^{CS,D} \rangle_{\mathbb{R}^6} + \left\langle \partial_{\bar{\mathbf{K}}^{CS}} \mathcal{H}_{p,v} | \dot{\bar{\mathbf{K}}^{CS}} \right\rangle_{\mathbb{R}^6 \times 6}, \quad (49)$$

where the second term corresponds to the change in energy due to varying the stiffness of the spring by the proportional law (40-41). In bond graph notation, the storage of the potential energy $\mathcal{H}_{p,v}$ is represented by a 2-port \mathbb{C} -element, as shown in Fig. 5.

By repeating the passivity analysis in Sec. III-C for the new impedance controller with stiffness modulation, one can easily show that the second term in (49) violates the passivity of the closed-loop system since it is a sign indefinite term. This can also be concluded easily by graphically inspecting the bond graph in Fig. 5 since the direction of the power supplied by the ‘‘stiffness modulation’’ module via the port $(\partial_{\bar{\mathbf{K}}^{CS}} \mathcal{H}_{p,v}, \dot{\bar{\mathbf{K}}^{CS}})$ is indefinite.

In conclusion, although the variable-stiffness impedance controller has the ability to regulate the interaction wrench, the contact stability is no longer guaranteed. In the next section, we solve this problem of the variable-stiffness impedance controller utilizing energy tanks and energy routing.

V. ENERGY-AWARE IMPEDANCE CONTROLLER

A way to restore the passivity, violated because of regulating the interaction wrench, is by using energy routing and energy tanks [10, 5]. The basic idea behind energy routing is that energy within the controller is directed from certain parts and stored in a virtual tank. This stored energy can then be used to implement the non-passive control action of wrench regulation. In this way, the total energy content of the closed-loop system remains unaffected. Thus, the contact stability of the aerial robot interacting with a passive environment is guaranteed again.

In what follows, we present the details of augmenting the impedance control with energy tanks and the effect it has on the overall closed-loop system’s passivity.

A. Idea of Energy Routing

In the modified controller augmented with an energy tank, the total spring wrench $\mathbf{W}_{\text{spr}}^{CS}$ of the impedance control law (30) will not be designed as in (43). Instead, the inclusion of the variable spring wrench $\mathbf{W}_{\text{spr},v}^{CS}$ will depend on whether

there is enough energy in the virtual tank to implement this non-passive control action or not. Therefore, instead of (43), the total spring wrench $\mathbf{W}_{\text{spr}}^{CS}$ is calculated by

$$\mathbf{W}_{\text{spr}}^{CS} = \mathbf{W}_{\text{spr},c}^{CS} + \mathbf{W}_{\text{reg}}^{CS}, \quad (50)$$

where $\mathbf{W}_{\text{reg}}^{CS} \in (\mathbb{R}^6)^*$ denotes the control wrench for regulating the interaction wrench, which is chosen as

$$\mathbf{W}_{\text{reg}}^{CS} = \alpha \mathbf{W}_{\text{spr},v}^{CS}, \quad (51)$$

where $0 \leq \alpha \leq 1$ is referred to as the *valve gain* which is regulated by the energy tank.

In normal operation when there is sufficient energy in the virtual tank available for wrench regulation, we have that $\alpha = 1$. Consequently, $\mathbf{W}_{\text{reg}}^{CS}$ is then equal to $\mathbf{W}_{\text{spr},v}^{CS}$ in (46) and the controller emulates the virtual spring with variable-stiffness. The power \mathcal{P}_{reg} that is required for regulating the interaction wrench is given by

$$\mathcal{P}_{\text{reg}} = (\mathbf{W}_{\text{reg}}^{CS})^\top \mathbf{T}_{CS}^{CS,D} = \alpha (\mathbf{W}_{\text{spr},v}^{CS})^\top \mathbf{T}_{CS}^{CS,D}. \quad (52)$$

This power is drawn from the energy tank, which is initialized by the control designer with a certain *energy budget* that is known a priori to be sufficient for achieving the desired interaction task. Once the energy tank depletes, it sets the valve gain α to zero and hence it follows that $\mathbf{W}_{\text{reg}}^{CS} = 0$. In this situation, the wrench regulation stops and the variable-stiffness spring is detached from the aerial robot.

If the depletion of the energy tank occurs before the interaction goal has been completely fulfilled, there could be two possibilities. One one hand, there could exist some sort of uncertainty during the interaction with the unknown environment that caused the depletion. In this case, the valve-based energy tank prevents the instabilities that could potentially occur due to continuation of the wrench regulation. On the other hand, it could be that the allocated energy budget was insufficient for the interaction task. In this case, a high-level strategy can be designed to analyze whether it is safe or not to allocate more energy in the tank to allow further regulation of the interaction wrench.

An important source of internal power that could be used to increase the energy stored in the virtual tank is the power dissipated by the virtual damper given by

$$\mathcal{P}_{\text{dmp}} = (\mathbf{W}_{\text{dmp}}^B)^\top \mathbf{T}_B^{B,I}, \quad (53)$$

which is always positive by construction. Instead of ‘‘throwing away’’ all of this power, only a certain portion of it \mathcal{P}_{dis} can be dissipated, which is given by

$$\mathcal{P}_{\text{dis}} = (1 - \eta) \mathcal{P}_{\text{dmp}}, \quad 0 < \eta \leq 1, \quad (54)$$

while the remainder, given by $\eta \mathcal{P}_{\text{dmp}}$ can be routed to the virtual tank to be stored. In this way, the energy dissipated by the virtual damper is exploited for implementing the wrench regulation.

Note that it is not advantageous to route all of the damper’s energy to the virtual tank (i.e. choose $\eta = 1$) since this will result in a lossless closed-loop system. Since a lossless system is on the border of passivity, choosing $\eta < 1$ allows for some passivity margin which could be beneficial in the presence of other passivity violation sources, such as modeling uncertainties and changing the virtual set-point during interaction.

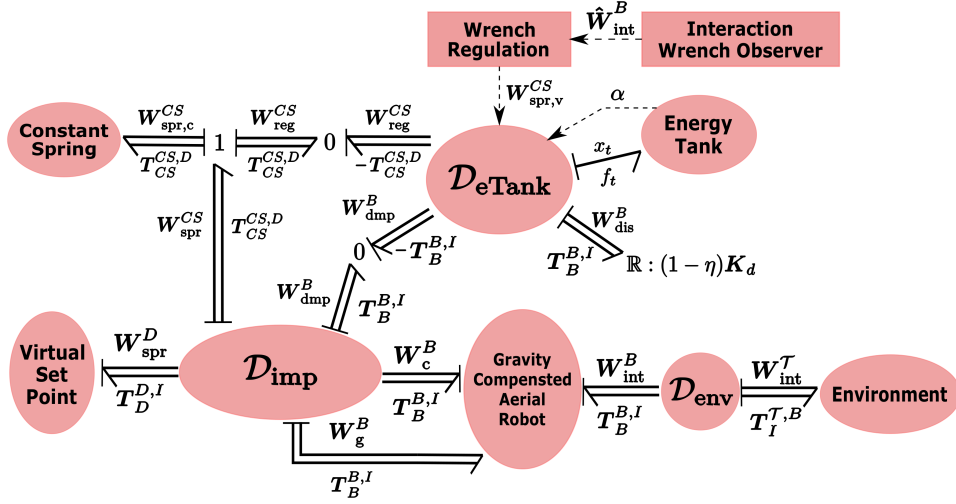


Figure 6: Port-based representation of the closed-loop system showing the energy-aware impedance controller which supplies the power needed for wrench regulation using an energy tank and the Dirac structure $\mathcal{D}_{e\text{Tank}}$ for energy routing.

B. Energy Routing using a Dirac Structure

The energy routing concept described above is implemented mathematically by the Dirac structure $\mathcal{D}_{e\text{Tank}}$ which mediates energy between four power ports, as shown in Fig. 6. The first port is $(\mathbf{W}_{\text{dmp}}^B, -\mathbf{T}_B^{B,I})$ which corresponds to $-\mathcal{P}_{\text{dmp}}$, while the second port is $(\mathbf{W}_{\text{dis}}^B, \mathbf{T}_B^{B,I})$ which corresponds to the dissipated power \mathcal{P}_{dis} , with its effort and flow variables related by the static relation

$$\mathbf{W}_{\text{dis}}^B = (1 - \eta) \mathbf{K}_d \mathbf{T}_B^{B,I}. \quad (55)$$

The third port is $(\mathbf{W}_{\text{reg}}^{CS}, -\mathbf{T}_{CS}^{CS,D})$ which corresponds to $-\mathcal{P}_{\text{reg}}$, while the fourth port is (x_t, f_t) with $x_t, f_t \in \mathbb{R}$ denoting the effort and flow variables of the energy tank and their product

$$\mathcal{P}_t := x_t f_t, \quad (56)$$

denoting the power entering the energy tank subsystem.

The Dirac structure $\mathcal{D}_{e\text{Tank}}$ connecting the aforementioned ports is defined as the relation corresponding to the skew-symmetric map given by

$$\begin{pmatrix} \mathbf{W}_{\text{reg}}^{CS} \\ \mathbf{W}_{\text{dmp}}^B \\ \mathbf{T}_B^{B,I} \\ f_t \end{pmatrix} = \mathcal{J}_{e\text{Tank}} \begin{pmatrix} -\mathbf{T}_{CS}^{CS,D} \\ -\mathbf{T}_B^{B,I} \\ \mathbf{W}_{\text{dis}}^B \\ x_t \end{pmatrix}, \quad (57)$$

$$\mathcal{J}_{e\text{Tank}} := \begin{pmatrix} \mathbf{0} & \mathbf{0} & \mathbf{0} & \frac{\alpha}{x_t} \mathbf{W}_{\text{spr},v}^{CS} \\ \mathbf{0} & \mathbf{0} & \mathbf{I}_6 & \frac{\eta}{x_t} \mathbf{K}_d \mathbf{T}_B^{B,I} \\ \mathbf{0} & -\mathbf{I}_6 & \mathbf{0} & \mathbf{0} \\ -\frac{\alpha}{x_t} (\mathbf{W}_{\text{spr},v}^{CS})^\top & -\frac{\eta}{x_t} (\mathbf{K}_d \mathbf{T}_B^{B,I})^\top & \mathbf{0} & \mathbf{0} \end{pmatrix}.$$

The first equation in (57) implements the wrench regulation control law (51). The second equation can be expressed using (55) as

$$\begin{aligned} \mathbf{W}_{\text{dmp}}^B &= \mathbf{W}_{\text{dis}}^B + \eta \mathbf{K}_d \mathbf{T}_B^{B,I} \\ &= (1 - \eta) \mathbf{K}_d \mathbf{T}_B^{B,I} + \eta \mathbf{K}_d \mathbf{T}_B^{B,I} = \mathbf{K}_d \mathbf{T}_B^{B,I}, \end{aligned} \quad (58)$$

which recovers the virtual damper's wrench (27). The last equation in (57) corresponds to the flow entering the energy tank system, which can be expressed as

$$f_t = \frac{\alpha}{x_t} (\mathbf{W}_{\text{spr},v}^{CS})^\top \mathbf{T}_{CS}^{CS,D} + \frac{\eta}{x_t} (\mathbf{K}_d \mathbf{T}_B^{B,I})^\top \mathbf{T}_B^{B,I}. \quad (59)$$

The energy balance encoded in the Dirac structure corresponding to (57) is given by

$$x_t f_t + (\mathbf{W}_{\text{dis}}^B)^\top \mathbf{T}_B^{B,I} = (\mathbf{W}_{\text{reg}}^{CS})^\top \mathbf{T}_{CS}^{CS,D} + (\mathbf{W}_{\text{dmp}}^B)^\top \mathbf{T}_B^{B,I}, \quad (60)$$

which can be rewritten using (52-56) as

$$\begin{aligned} \mathcal{P}_t &= \mathcal{P}_{\text{reg}} + \mathcal{P}_{\text{dmp}} - \mathcal{P}_{\text{dis}} \\ &= \mathcal{P}_{\text{reg}} + \mathcal{P}_{\text{dmp}} - (1 - \eta) \mathcal{P}_{\text{dmp}} = \mathcal{P}_{\text{reg}} + \eta \mathcal{P}_{\text{dmp}}. \end{aligned} \quad (61)$$

The expression (61) states that the power flowing into the energy tank is the sum of the power needed for regulating the interaction wrench and a portion of the virtual damper's energy. While the direction of \mathcal{P}_{dmp} is always flowing from the damper to the tank, the flow of \mathcal{P}_{reg} can be in both directions.

In conclusion, the power-preserving Dirac structure corresponding to (57) implements the desired energy routing concept which directs the power required to implement the wrench regulation control action from the energy tank, while exploiting a portion of the virtual damper's energy to fill the energy tank and dissipate the remainder. As long as the energy tank includes sufficient energy, the wrench regulation is equivalent to the action of a variable-stiffness virtual spring.

C. Design of the Energy Tank

With reference to Fig. 7, the energy tank is represented by a storage element \mathbb{C} with its state $x_t \in \mathbb{R}$ and energy function E_t given by

$$E_t(x_t) = \frac{1}{2} x_t^2. \quad (62)$$

By construction, one has that the flow and effort variables of the storage element to be given by $\dot{x}_t \in \mathbb{R}$ and $\partial_{x_t} E_t = x_t \in \mathbb{R}$, respectively.

The energy tank is designed such that, in addition to energy storage, it adheres to two important behaviors. First, the level of energy in the tank should never reach zero as this implies that $x_t = 0$ which would create a singularity in (59) and (51). Therefore, the tank energy should never drop below a pre-specified lower limit E_t^- . This can be enforced by setting the

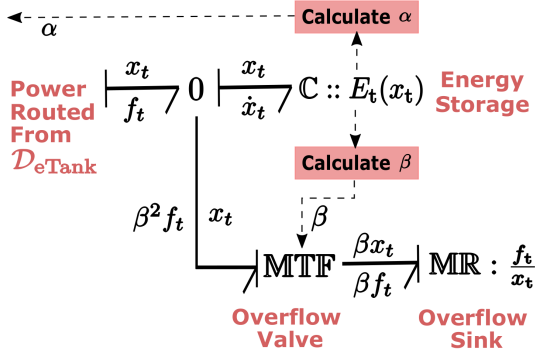


Figure 7: Port-based representation of the energy tank.

valve gain $\alpha = 0$ when $E_t \leq E_t^-$ and $\alpha = 1$ otherwise. To avoid discontinuities in (59) and (51) and the consequent chattering in the robot's control signals, the transition between 0 and 1 can be made smooth, as suggested by [25]:

$$\alpha = \begin{cases} 0 & \text{if } E_t \leq E_t^- \\ \frac{1}{2} \left[1 - \cos \left(\frac{E_t - E_t^-}{\delta E} \pi \right) \right] & \text{if } E_t^- < E_t < (E_t^- + \delta E) \\ 1 & \text{otherwise,} \end{cases} \quad (63)$$

for some $\delta E > 0$.

Second, the maximum level of energy in the tank should be limited to avoid a steady increase of E_t . In this way, the energy budget allocated to perform the wrench regulation can be kept under control. This maximum energy level allowed in the tank E_t^+ can be enforced by the use of an overflow valve and sink implemented using a modulated transformer and modulated resistive element, as shown in Fig. 7.

The flow variables of the three ports connected by the zero-junction in Fig. 7 satisfy the condition

$$\dot{x}_t = f_t - \beta^2 f_t = (1 - \beta^2) f_t. \quad (64)$$

By multiplying both sides of (64) we have that the power stored in the tank (i.e. $\dot{E}_t = x_t \dot{x}_t$) and the power directed from $\mathcal{D}_{e\text{Tank}}$ (i.e. $\mathcal{P}_t = x_t f_t$) are related by

$$\dot{E}_t = (1 - \beta^2) \mathcal{P}_t, \quad (65)$$

where $\beta \in \{0, 1\}$ is a scalar that represents the state of the overflow valve calculated by

$$\beta = \begin{cases} 1 & \text{if } E_t \geq E_t^+ \text{ \& } \mathcal{P}_t > 0, \\ 0 & \text{otherwise.} \end{cases} \quad (66)$$

In this way, all the power that is routed from $\mathcal{D}_{e\text{Tank}}$ is stored in the energy tank when $\beta = 0$. Whereas, when $\beta = 1$, all the power routed is dissipated by the modulated resistor and the maximum of E_t is ensured to be E_t^+ . Thus, the MITF emulates a virtual overflow valve. Note that the discontinuity of β in (66) will only affect the power stored in the C-element and will cause no chattering to the control signals of the robot.

D. Passivity Analysis of the Closed-loop System

Finally, we conclude this section with an analysis of the passivity of the closed loop system shown in Fig. 6. Recall that the passivity of the closed loop system is assessed by

ensuring that the total energy stored in the system is non-increasing. Such assessment is straightforward by graphical inspection of the bond graph in Fig. 6, which eliminates the need of an analytic proof of passivity.

The closed-loop system (excluding the environment) consists of five dynamical systems that are interconnected together: 1) the gravity compensated aerial robot, 2) the constant virtual spring, 3) the resistive element, 4) the virtual set-point generator, and 5) the energy tank. Other modules in the system consists of the power ports, junctions, Dirac structures, and the *signal processing* parts of the controller that include the interaction wrench regulation and observer algorithms.

All the power ports, junctions, and Dirac structures are power-preserving by construction. In other words, they only route the power flowing through them without increasing or decreasing the total power. As for the signal-processing modules, they are connected such that they do not inject energy into system but instead modulate the Dirac structure $\mathcal{D}_{e\text{Tank}}$. Therefore, a sufficient condition for the overall system's passivity is to ensure that each of its individual dynamical subsystems is passive

By construction, we have that the constant spring, the resistive element, and the energy tank are all passive dynamical systems, whereas the environment is passive by assumption. As for the gravity compensated aerial robot, it is passive under the assumption of perfect gravity compensation. As for the virtual set-point generator, similar to Sec. III-C, under the assumption that the virtual set-point Ψ_D changes during physical interaction in a piece-wise constant or quasi-static manner such that the power injected is less than that dissipated i.e.

$$-(\mathbf{W}_{\text{spr}}^D)^\top \mathbf{T}_D^{D,I} < (1 - \eta) (\mathbf{T}_B^{B,I})^\top \mathbf{K}_d \mathbf{T}_B^{B,I}, \quad (67)$$

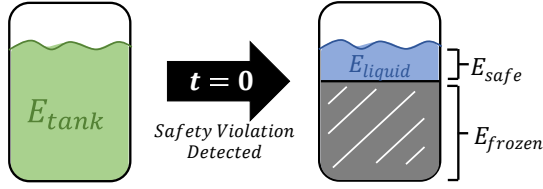
then the it does not violate the passivity.

In conclusion, with the above graphical inspection of Fig. 6, the contact stability between any passive environment and the aerial robot controlled by the proposed energy-aware impedance controller is guaranteed. Thanks to the port-based representation of the system dynamics, we are able to assess the system's passivity just by graphical observation without lengthy power inequalities usually encountered in analytical passivity checks.

VI. TOWARDS SAFE INTERACTION: A SAFETY EXTENSION FOR ENERGY TANKS

Next to achieving *stable* contact of a flying end-effector with the environment, another goal of our work is to find a way to ensure a certain level of safety during the interaction. The safety issue we address arises when the end effector of the MAV loses contact while trying to regulate a commanded interaction wrench, inspired by [18]. We also aim for a solution that is effective in a multitude of scenarios, without having to adapt it to the specific scenario.

We propose a safety algorithm that exploits the energy tank as an observer for the amount of energy needed to regulate the wrench with the unknown and unobserved environment. Therefore to ensure safe interaction, the energy-tank can be

Figure 8: Illustration of the *energy freezing* concept.

extended to enforce stricter limitations to the amount of power the wrench regulator can draw from the tank.

The first step in our strategy relies on tracking the amount of power that is drawn due to wrench regulation (\mathcal{P}_{reg}). In case of contact loss, a high amount of energy will be drawn from the tank within a short amount of time, which can subsequently be detected as a *safety violation*. A basic method for performing such a detection is to simply put a threshold on \mathcal{P}_{reg} , where the threshold will be referred to as $\mathcal{P}_{\text{unsafe}}$. Thus, we have that

$$\text{Safety Violation} = \begin{cases} \text{True} & \text{if } \mathcal{P}_{\text{reg}} > \mathcal{P}_{\text{unsafe}} \\ \text{False} & \text{else} \end{cases} \quad (68)$$

Next, based on the detected power surge, one strategy would be to immediately shut off the wrench regulator. However, such naive strategy would be highly sensitive to sensor noise if the threshold is placed sufficiently low, leading to chattering in the actuators of the MAV. Instead, we introduce an implicit hysteresis in the energy tank by limiting the available energy in the tank after a detected safety violation. We refer to this novel extension of energy tanks by *energy freezing and melting*, summarized in Alg. 1.

With reference to Fig. 8, the intuition behind this process is to *freeze* a large part of the energy in the tank as soon as a safety violation is detected. This frozen part (E_{frozen}) will not be usable, only the liquid energy (E_{liquid}) left behind can be used for implementing the desired control task, i.e. the interaction wrench regulation. This liquid amount of energy is initialized to be a user-specific amount E_{safe} . Thus, the valve gain α in (63) is calculated using E_{liquid} instead of E_t .

In case the safety violation detection is a true positive, the energy allowed for wrench regulation is limited to E_{safe} by construction. However, in case of a false positive *Safety Violation*, e.g. due to spikes in \mathcal{P}_{reg} resulting from high sensor noises or sudden environment disturbances, the algorithm *melts* the frozen energy in the tank such that it can be used for wrench regulation again. In this manner, the actual energy content in the tank is not altered, such that the passivity of the system is maintained. The rate at which E_{frozen} is melted over time is determined by the $\gamma_{\text{melt}} \in \mathbb{R}^+$ parameter. To prevent that energy melting occurs during actual contact loss, the melting process is stopped if the safety extension actually starts responding, which is when $\alpha < 1$. In addition, it should also be made sure that E_{frozen} does not drop below the minimum tank energy E_t^- .

A summary of our energy-tank safety extension can be found in Algorithm 1.

Algorithm 1: Energy Freezing & Melting Algorithm

Inputs: E_t , *Safety Violation*
Outputs: α
Parameters: E_{safe} , E_t^- , δE , γ_{melt}
Variables: E_{frozen} , E_{liquid}
Initialize: $E_{\text{frozen}} = E_t^-$;

// Freezing:

if *Safety Violation* **and** $E_t - E_{\text{safe}} > E_{\text{frozen}}$ **then**

| $E_{\text{frozen}} = E_t - E_{\text{safe}}$;

end

// Output:

 $E_{\text{liquid}} = E_t - E_{\text{frozen}}$;

Calculate α from (63) using E_{liquid} instead of E_t ;

// Melting:

if $E_{\text{frozen}} > E_t^-$ **and** $\alpha == 1$ **then**

| $\dot{E}_{\text{frozen}} = -\gamma_{\text{melt}}$;

else

| $\dot{E}_{\text{frozen}} = 0$;

end

VII. EXTENSIVE VALIDATION OF THE CONTROLLER

In this section, we present the validation campaign that we conducted to validate the proposed energy aware impedance control strategy for a flying end-effector. We extensively tested such controller by means of both realistic numerical simulations using 20Sim [42] and Gazebo/RotorS [43] as well as real experiments, in different scenarios and operational conditions. Due to space limitation, we are going to present here the results of the experimental tests. However, we believe the simulation results to be a valuable complement to the experimental outcomes described in this paper. Therefore, for completeness and clarity of exposition, we sketch in Tab. II an overview of the simulation environment and the goal for each simulation test, while the interested reader is referred to [44] for a complete description of these tests.

After a brief outline of our experimental setup, we present and discuss the results of five different real scenarios which we chose to highlight the most representative key-features of our method. An overview of the indoor environment and the goal for each experimental test is gathered in Tab. III.

A. Experimental setup

The aerial robot employed for the experimental validation is a custom-made fully-actuated hexarotor, cf. Fig. 9. As

Table II: Summary of the simulation results in [44].

Scenario	Environment	Goal
s-I	20Sim & Gazebo/RotorS	Validate the energy-aware controller showing that <i>passivity</i> (and thus stability) is ensured
s-II	20Sim	Validate the behavior of the energy-aware controller when the energy tank is <i>depleted</i>
s-III	20Sim & Gazebo/RotorS	Validate the energy-tank safety extension in the event of a <i>translational</i> contact-loss
s-IV	20Sim	Validate the energy-tank safety extension in the event of a <i>rotational</i> contact-loss
s-V	20Sim & Gazebo/RotorS	Tune the behavior of the energy-tank safety extension in the event of a <i>false contact-loss</i> detection due to sensor noise



(a) Indoor flight-lab



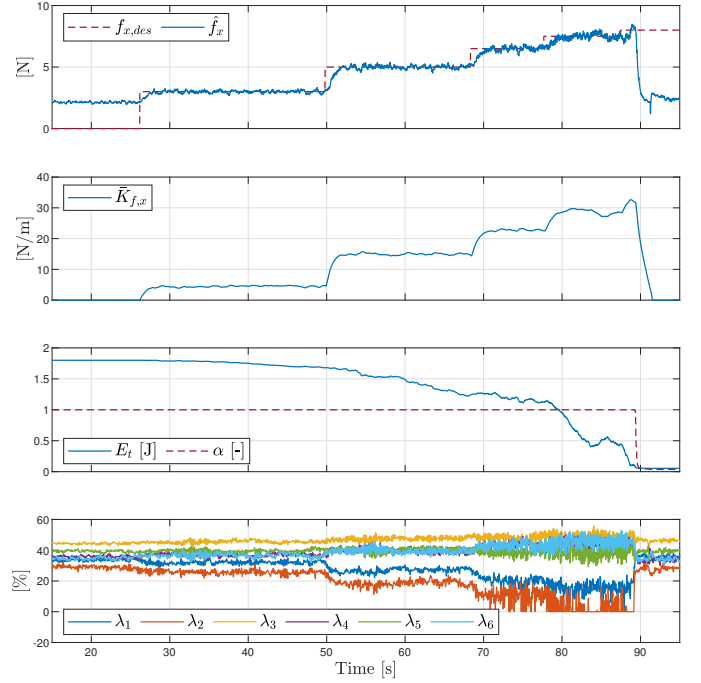
(b) Indoor arena

Figure 9: The fully-actuated hexarotor aerial robot in two different environments.

already mentioned, the assumption of full-actuation is crucial in order to be able to control the interaction wrench at will, cf. \mathbf{W}_c^B in (11), which is always possible within the limits of the actuators, assumed to be the nominal working condition. A thorough description of the physical parameters of the robot as well as technical details on the software architecture and the sensors used in the experiments can be found in [45]. The demonstrations took place in two indoor environments endowed with motion capture systems to provide reliable estimates of the robot configuration and twist, as the contributions of the paper are clearly focused on control rather than perception: scenarios e-I – e-III were performed in a small flight lab ($4.33 \times 2.81 \times 2.62\text{m}$), while scenarios e-IV – e-V were carried out in a larger indoor arena ($7.43 \times 5.93 \times 5.93\text{m}$). The choice of different surrounding conditions is motivated by the will of preliminarily assessing the influence of different external environments on the controlled aerial system and by the need of repeatably performing challenging tests in safe conditions. Unless otherwise stated, the values of the energy

Table III: Overview of the presented experimental results.

Scenario	Environment	Goal
e-I	Indoor lab	Validate the behavior of the energy-aware controller when the energy tank is <i>depleted</i>
e-II	Indoor lab	Compare the interaction controller performance for <i>different energy routing configurations</i> by changing η
e-III	Indoor lab	Showcase the aerial robot's ability to regulate the interaction wrench with <i>different orientations</i>
e-IV	Indoor arena	Highlight the consequences of using the <i>variable impedance controller</i> (without energy-tanks) in the event of a translational <i>contact-loss</i>
e-V	Indoor arena	Validate the behavior of the energy-aware controller (with <i>safety extension</i>) in the event of a translational <i>contact-loss</i>

Figure 10: Plots related to Scenario e-I. From top to bottom, the tracking of the reference interaction wrench, the actively-regulated value of the variable-spring stiffness along f_x , the level of energy stored in tank together with the value of the α valve gain (63), and the actuator PWM commands.

tank parameters for all the presented experiments are $\eta = 0$, $E_t^- = 0.05$, $E_t^+ = 1.8$, $\delta E = 0.03$, $\gamma_{\text{melt}} = 0.2$, $\mathcal{P}_{\text{unsafe}} = 0.3$, $E_{\text{safe}} = 0.04$.

The interested reader can find the footage of the presented experiments in the supplementary video.

B. Scenario e-I: wrench regulation and tank depletion

The goal of this experiment is twofold: assess the correct execution of the wrench regulation under normal operation, and validate the behavior of the energy-aware impedance/wrench controller (without safety extension) when the energy tank is depleted. During this scenario, the MAV is commanded to exert a reference force on a fixed vertical surface placed in the flight lab. The desired force is along the \hat{x}_E axis of the end-effector's frame Ψ_E which is chosen collinear with the end-effector's forward direction.

As shown in the first and the third plots of Fig. 10, the piece-wise constant reference force is properly tracked by the controller as long as the level of energy in the tank is higher than the lower limit E_t^- . Such a proper wrench tracking is achieved by modulating the stiffness of the virtual spring, whose evolution is depicted in the second plot, following (40). In particular, it is worth mentioning that during the initial phase of the experiment (until $t \approx 27\text{s}$) the wrench tracking is not enabled in the control (the user can trigger this behavior via a user-interface), therefore the spring stiffness is regulated to zero despite the non-zero sensed force due to the contact.

On the other hand, as soon as the energy tank is depleted ($t \approx 89\text{s}$), the value of the valve gain α is automatically brought from 1 to 0 in a continuous fashion, following (63). As

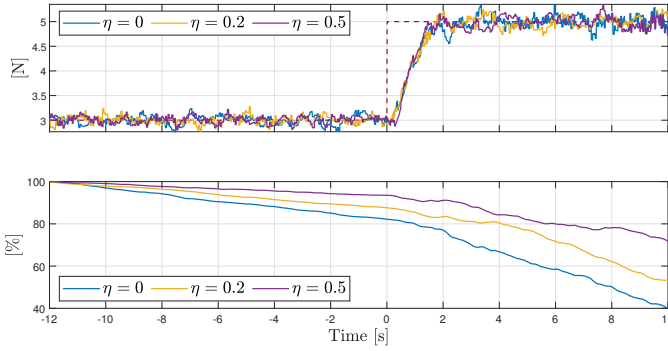


Figure 11: Plots related to Scenario e-II. Top: interaction force regulation for different values of the η parameter (54). Bottom: level of energy in the tank for the same η values.

a consequence, the control wrench for regulating the interaction, cf. (51), drops to 0 as well, producing the expected cease in the wrench tracking, which is desirable to prevent potential instabilities issues arising from an unrestrained interaction. This demonstrates the effectiveness of the energy awareness of the proposed impedance controller. In particular, it should be appreciated how the transition between the two desired behaviors occurs in a stable manner without theoretically violating the passivity of the system.

Finally, two main observations should be drawn from the last plot of Fig. 10: first, increasing the desired interaction force requires enlarging span in the actuator velocities (due to the tilting of the propellers) and, second, the MAV remains stable despite the saturation of one actuator for almost 20 seconds, which highlights the robustness of the presented controller.

C. Scenario e-II: different energy-routing configurations

In this scenario, we want to show the performance of the controller (without safety extension) in terms of wrench regulation and energy consumption when operating with different energy-routing configurations, i.e., when changing the value of η in (54), which indicates the percentage of energy dissipated by the virtual damper which is re-injected in the energy tank.

It should be expected that, if the robot is performing the same task in very similar conditions, the level of energy in the tank should decrease more slowly for increasing values of η , since a larger portion of the dissipated energy is refilled in the tank and can be re-used for pursuing the task execution for a longer nominal time. This intuition is confirmed by the second plot of Fig. 11, which shows that the average slope of the tank level decreases, in absolute value, for increasing values of η . At the same time, it should be noted that smaller η values provide more robustness in case of unexpected events, because the robot would stop the wrench regulation in advance.

On the other hand, the quality of the wrench regulation is independent from the particular value of such tuning parameter, as shown in the first plot of Fig. 11. Indeed, when the reference contact force changes, the regulated one converge to new desired value with indistinct behaviors in the three cases.

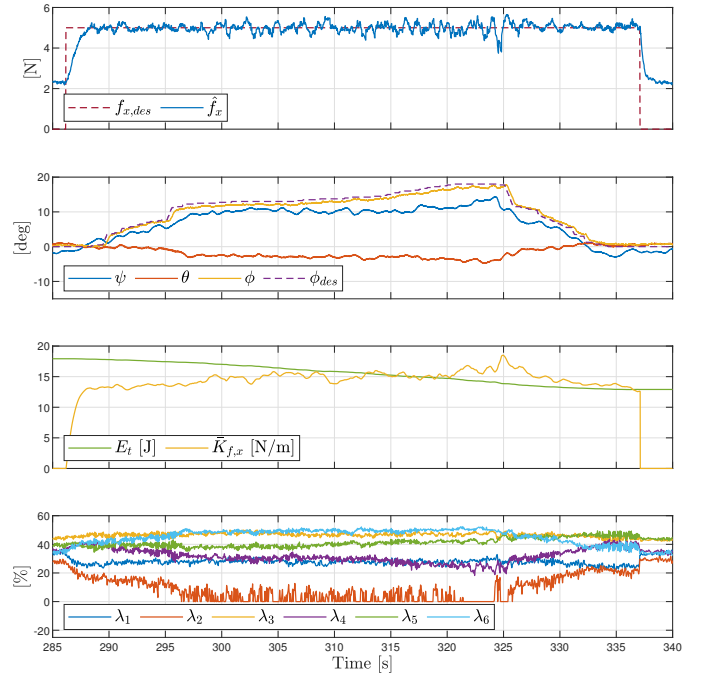


Figure 12: Plots related to Scenario e-III. From top to bottom, the tracking of the reference interaction wrench, the tracking of the orientation reference, the level of energy stored in tank together with the actively-regulated value of the variable-spring stiffness along f_x , and the rotor PWM commands.

Therefore, this experiment shows how the wrench can be seamlessly regulated for different values of the gain η , depending on the required robustness of the closed-loop system.

D. Scenario e-III: full-actuation MAV capability

With this experiment, we want to showcase the capability of the flying robot, controlled with the proposed energy-aware method, to track the reference interaction wrench in multiple ways, namely with different orientations.

During this demonstration, the MAV is required to exert a constant force along \hat{x}_E of 4.5N on a fixed vertical surface placed in the flight lab, while the user changes the desired robot's roll angle (ϕ_{des}) at the same time. As shown in the first and the second plot of Fig. 12, where the robot orientation is displayed with a minimal yaw(ψ)-pitch(θ)-roll(ϕ) representation for the reader's convenience, the interaction force is effectively regulated and maintained even when the robot is considerably tilted w.r.t. the horizontal plane. This capability becomes particularly useful when the MAV is operating in cluttered environments, since the wrench tracking can be ensured while simultaneously performing obstacle avoidance or other secondary tasks.

It is important to note that while only the desired roll is commanded to a non-zero value, the actual robot's pitch and yaw angles change also as a by-product. This behavior is due to the fact that they are automatically adjusted by the controller to precisely ensure the force regulation even with the saturation of one actuator is reached, as shown in the fourth plot. Such behavior is a key difference between the paradigm of impedance/behavior control, compared to for

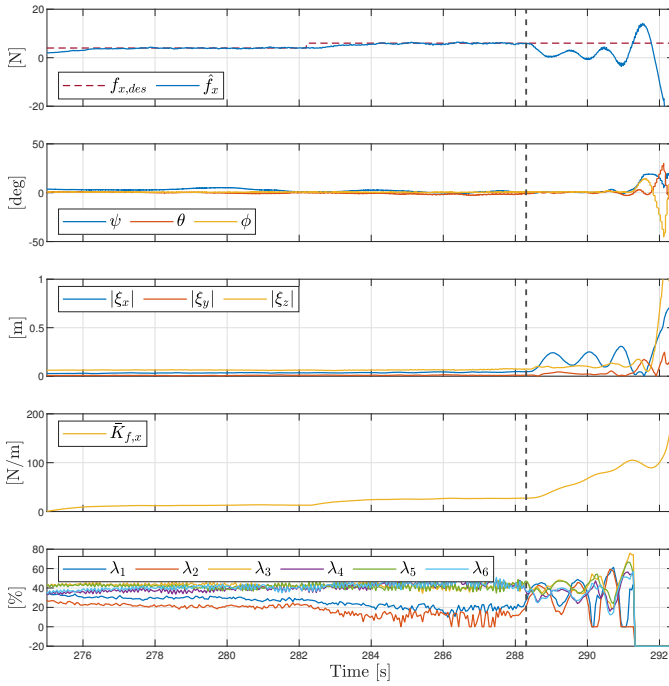


Figure 13: Plots related to Scenario e-IV. From top to bottom, the tracking of the reference interaction wrench, the tracking of the orientation reference, the linear extension of the virtual spring, the actively-regulated value of the variable-spring stiffness along f_x , and the rotor PWM commands.

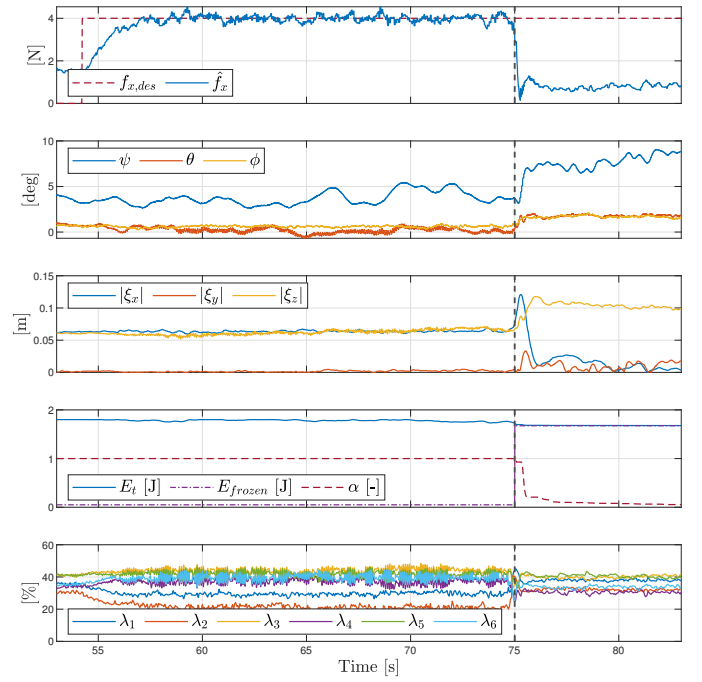


Figure 14: Plots related to Scenario e-V. From top to bottom, the tracking of the reference interaction wrench, the tracking of the orientation reference, the linear extension of the spring, the level of energy stored in tank together with the value of the α valve gain (63), and the rotor PWM commands.

example hybrid pose-wrench control, where one controls the behavior of the robot instead of exact control of its states. By increasing the rotational stiffness of the geometric spring, the deviation in the pitch and yaw angles can be decreased.

Furthermore, from the third plot it can be appreciated that the level of energy in the tank, this time initialized to $E_t^+ = 18\text{J}$ to allow for longer operational time, decreases throughout the task execution also in this scenario. The stiffness of the virtual spring is actively regulated using the feedback coming from the wrench sensing, as usual. Finally, it is clear from the fourth plot that the robot maintains its stability despite the saturation of one actuator, which demonstrates again the robustness of the controller.

E. Scenario e-IV: importance of energy awareness

In this fourth experiment, the main goal is to stress the importance of the energy awareness embedded in the presented energy tank based controller by showing the possible consequences of using instead an energy agnostic controller to accomplish interaction tasks in challenging situations, e.g. when a contact-loss occurs during the interaction. To showcase this, we used the variable stiffness controller described in Sec. IV, which does not contain any of the augmentations presented in Sec. V–VI, and generated a translational contact-loss in a simple but repeatable way, mounting a vertical surface on a cart, as shown in Fig. 9 and the supplementary video.

During this test, the MAV was tasked to regulate a piecewise constant force along \hat{x}_E on the vertical surface, which was blocked during the first part of the experiment and then moved to produce the contact loss. The plots of the key results

are collected in Fig. 13, where the vertical black line denotes the moment in which the cart was moved. As soon as the lateral constraint provided by the wall is removed from the robot end effector, the latter starts to oscillate around the resting position of the virtual spring behaving like a mass-spring-damper system, as it can be appreciated from the third plot. However, since the wrench tracking is still enabled and the sensed force drops to zero due to the lack of contact, cf. the first plot, an increase is triggered in the stiffness of the virtual spring (40), as shown in the fourth plot. This causes the amplitude of the oscillations, which would otherwise remain at most constant (some damping is present), to increase, leading to the instability of the robot, cf. the second and third plots. As a matter of fact, the experiment had to be aborted (shown in approx. the last one second of the plots in Fig. 13).

This experimental result highlights the importance of energy-awareness. Indeed, since this controller is energy agnostic, it does not observe the energy flow related to the wrench regulation, and thus it couldn't regulate the interaction wrench as done in (40). If the energy-tank extension described in Sec. V was instead used, the wrench regulation would have been stopped once the tank depletion was reached, as demonstrated in scenario e-I. However, it should be appreciated that, even before reaching instability the behavior of the robot is not safe due its high oscillations, which we would like to avoid in the first place by monitoring the energy and the power extracted from the tank.

F. Scenario e-V: energy-aware contact-loss stabilization

In this last scenario, we repeated the previous experiment activating the energy-tank with the safety extension presented in Sec. VI. In this case, the controller becomes aware of the contact loss (occurring at $t \approx 75$ s) by detecting a violation in the maximum power that can be extracted from the tank, whose value has been tuned in preliminary tests. As shown by the fourth plot of Fig. 14, the abrupt extraction of energy from the tank due to the contact-loss (not obvious from the figure due to the reduced sample frequencies for the plots) causes the freezing of most of the energy in the tank, made possible by the safety extension detailed in Alg. 1. As a consequence, the valve gain α is closed, as already validated in e-I, and the wrench tracking is discontinued, as we can see in the first plot. For this experiment, we used $E_{\text{safe}} = E_t^-$. By comparing the third plots of Figs 13 and 14, it is clear how the robot end-effector does not oscillate like in previous case but instead quickly converge the resting position of the virtual spring. It is worth mentioning that the offset in the vertical distance $|\xi_z|$ is due to non-perfect gravity compensation and external disturbances from the power cables, as depicted in Fig. 9.

Indeed, thanks to its energy awareness, the controller can monitor the amount of energy and power extracted from the tank, and can properly react to this, which validates the success of the proposed safety extension. This concludes the validation of the proposed controller.

VIII. FURTHER EVALUATION AND DISCUSSION

In this section we discuss some general issues and limitations of our proposed interaction control framework presented in this paper.

First, an important issue that was observed in validating the controller experimentally is the fact that, during the wrench regulation, the rate at which the energy in the tank decreases/increases depends on the environment. The reason behind this dependency can be seen from the power required for wrench regulation in (52) which depends on the twist of the MAV that is affected not only by the interaction target but also aerodynamic disturbances, power-cable disturbances, and non-modeled dynamics.

Second, compared to the safety extension proposed in [18], the port-Hamiltonian formalism used in this work allows to reason just in terms of energy and power extraction from the tank, thus allowing to react to different heterogeneous situations like, e.g., a rotational contact-loss, in a general way as shown in the simulations of [44]. Furthermore, the control-by-interconnection approach used has the benefit of being modular which allows upgrading some subsystems of the control system e.g. the stiffness adaptive law or the wrench observer, for performance enhancement.

Finally, in this work we highlighted the concept of “energy-awareness” and its benefit for modeling and control of interactive robots in general [5]. The use of virtual tanks allowed for means to be aware of the energy used to regulate the interaction wrench which violated the system’s passivity. By exploiting the estimated energy budget allowed for accomplishing the task and (optionally) the dissipated free energy

in the controller, the energy tank prevents the injection of an uncontrolled amount of energy into the system, which could lead to instability. Furthermore, this awareness of the energy flow was shown useful also in enabling safe interaction between the robot and its environment.

IX. CONCLUSION AND FUTURE WORK

This paper presented an enhanced impedance control system, derived in the port-Hamiltonian framework, capable of regulating the interaction wrench of a flying end-effector while ensuring stable and safe physical interaction with the environment. Furthermore, the advantages of the energy aware control approach presented goes beyond standard passivity-based control techniques in ensuring both *stable and safe* physical interaction. From a system-theoretic point of view, a passive system only stores or dissipates energy which implies stability. From a practical point of view, if the stored energy is huge, it could possibly be transformed into high kinetic energy of the robot leading subsequently to high-impact collisions. However, by utilizing the awareness of the energy flow within the controller, high-level algorithms could be designed to ensure additional safety requirements.

As a future continuation of the energy-aware interaction framework proposed, an important question that has not been tackled here is: how to determine the energy budget allocated to the virtual tank? This design parameter of the energy-aware controller has a significant effect on its behavior. If a low energy budget is allocated, then the interaction task can not be fulfilled, whereas a high energy budget could potentially lead to an unsafe interaction.

One potential solution is to rely on online sampling-based approximations of the environment to estimate the required budget for normal operation combined with machine learning techniques to optimize this budget during the task.

REFERENCES

- [1] M. Ryll, G. Muscio, F. Pierri, E. Cataldi, G. Antonelli, F. Caccavale, D. Bicego, and A. Franchi, “6D interaction control with aerial robots: The flying end-effector paradigm,” *The International Journal of Robotics Research*, vol. 38, no. 9, pp. 1045–1062, 2019.
- [2] F. Ruggiero, V. Lippiello, and A. Ollero, “Aerial manipulation: A literature review,” *IEEE Robotics and Automation Letters*, vol. 3, no. 3, pp. 1957–1964, 2018.
- [3] A. Ollero, G. Heredia, A. Franchi, G. Antonelli, K. Kondak, A. Sanfeliu, A. Viguria, J. R. Martinez-de Dios, F. Pierri, J. Cortés, *et al.*, “The AEROARMS project: Aerial robots with advanced manipulation capabilities for inspection and maintenance,” *IEEE Robotics & Automation Magazine*, vol. 25, no. 4, pp. 12–23, 2018.
- [4] S. Park, J. Lee, J. Ahn, M. Kim, J. Her, G.-H. Yang, and D. Lee, “Odor: Aerial manipulation platform enabling omnidirectional wrench generation,” *IEEE/ASME Transactions on Mechatronics*, vol. 23, no. 4, pp. 1907–1918, 2018.
- [5] S. Stramigioli, “Energy-aware robotics,” in *Mathematical Control Theory I*. Springer, 2015, pp. 37–50.
- [6] —, *Modeling and IPC Control of Interactive Mechanical Systems - A Coordinate-Free Approach*. Springer-Verlag London, 2001.
- [7] N. Hogan, “Impedance control: An approach to manipulation: Part I-Theory,” *Journal of Dynamic Systems, Measurement and Control*, vol. 107, no. 1, pp. 1–7, 1985.
- [8] —, “Impedance control: An approach to manipulation: Part II-Implementation,” *Journal of Dynamic Systems, Measurement and Control*, vol. 107, no. 1, pp. 8–16, 1985.
- [9] —, “Impedance control: An approach to manipulation: Part III-Applications,” *Journal of Dynamic Systems, Measurement and Control*, vol. 107, no. 1, pp. 17–24, 1985.

- [10] V. Duindam and S. Stramigioli, "Port-based asymptotic curve tracking for mechanical systems," *European Journal of Control*, vol. 10, no. 5, pp. 411–420, 2004.
- [11] J. Cervera, A. J. van der Schaft, and A. Baños, "Interconnection of port-hamiltonian systems and composition of Dirac structures," *Automatica*, vol. 43, no. 2, pp. 212–225, 2007.
- [12] L. Villani and J. De Schutter, "Force control," in *Springer handbook of robotics*. Springer, 2016, pp. 195–220.
- [13] R. Rashad, J. Goerres, R. G. Aarts, J. B. Engelen, and S. Stramigioli, "Fully Actuated Multirotor UAVs: A Literature Review," *IEEE Robotics and Automation Magazine*, vol. 27, no. 3, pp. 97 – 107, 2020.
- [14] E. D. Fasse and J. F. Broenink, "A spatial impedance controller for robotic manipulation," *IEEE Transactions on Robotics and Automation*, vol. 13, no. 4, pp. 546–556, 1997.
- [15] E. D. Fasse, "On the Spatial Compliance of Robotic Manipulators," *Journal of Dynamic Systems, Measurement and Control*, vol. 119, no. 4, pp. 839–844, 1997.
- [16] S. Stramigioli and V. Duindam, "Variable spatial springs for robot control applications," *IEEE/RSJ Int. Conf. Intell. Robot. Syst.*, vol. 4, pp. 1906–1911, 2001.
- [17] R. Rashad, F. Califano, and S. Stramigioli, "Port-Hamiltonian passivity-based control on SE(3) of a fully actuated UAV for aerial physical interaction near-hovering," *IEEE Robotics and Automation Letters*, vol. 4, no. 4, pp. 4378–4385, 2019.
- [18] C. Schindlbeck and S. Haddadin, "Unified passivity-based cartesian force/impedance control for rigid and flexible joint robots via task-energy tanks," in *IEEE International Conference on Robotics and Automation (ICRA)*. IEEE, 2015, pp. 440–447.
- [19] F. Ferraguti, C. Secchi, and C. Fantuzzi, "A tank-based approach to impedance control with variable stiffness," in *IEEE International Conference on Robotics and Automation (ICRA)*. IEEE, 2013, pp. 4948–4953.
- [20] F. Ferraguti, N. Preda, A. Manurung, M. Bonfe, O. Lambercy, R. Gassert, R. Muradore, P. Fiorini, and C. Secchi, "An energy tank-based interactive control architecture for autonomous and teleoperated robotic surgery," *IEEE Transactions on Robotics*, vol. 31, no. 5, pp. 1073–1088, 2015.
- [21] R. Rashad, J. B. Engelen, and S. Stramigioli, "Energy tank-based wrench/impedance control of a fully-actuated hexarotor: A geometric port-Hamiltonian approach," in *IEEE International Conference on Robotics and Automation (ICRA)*. IEEE, 2019, pp. 6418–6424.
- [22] A. Dietrich, X. Wu, K. Bussmann, C. Ott, A. Albu-Schaffer, and S. Stramigioli, "Passive Hierarchical Impedance Control Via Energy Tanks," *IEEE Robotics and Automation Letters*, vol. 2, no. 2, pp. 522–529, apr 2017.
- [23] G. Raiola, C. A. Cardenas, T. S. Tadele, T. de Vries, and S. Stramigioli, "Development of a safety-and energy-aware impedance controller for collaborative robots," *IEEE Robotics and Automation Letters*, vol. 3, no. 2, pp. 1237–1244, 2018.
- [24] T. S. Tadele, T. J. De Vries, and S. Stramigioli, "Combining energy and power based safety metrics in controller design for domestic robots," in *2014 IEEE International Conference on Robotics and Automation (ICRA)*. IEEE, 2014, pp. 1209–1214.
- [25] E. Shahriari, L. Johannsmeier, and S. Haddadin, "Valve-based virtual energy tanks: A framework to simultaneously passify controls and embed control objectives," in *American Control Conference (ACC)*. IEEE, 2018, pp. 3634–3641.
- [26] M. Orsag, C. Korpela, S. Bogdan, and P. Oh, "Dexterous aerial robots-mobile manipulation using unmanned aerial systems," *IEEE Transactions on Robotics*, vol. 33, no. 6, pp. 1453–1466, 2017.
- [27] G. Nava, Q. Sablé, M. Tognon, D. Pucci, and A. Franchi, "Direct force feedback control and online multi-task optimization for aerial manipulators," *IEEE Robotics and Automation Letters*, vol. 5, no. 2, pp. 331–338, 2019.
- [28] A. Y. Mersha, S. Stramigioli, and R. Carloni, "Variable impedance control for aerial interaction," *IEEE Int. Conf. Intell. Robot. Syst.*, pp. 3435–3440, 2014.
- [29] A. Suarez, G. Heredia, and A. Ollero, "Physical-Virtual Impedance Control in Ultralightweight and Compliant Dual-Arm Aerial Manipulators," *IEEE Robot. Autom. Lett.*, vol. 3, no. 3, pp. 2553–2560, jul 2018.
- [30] T. Lee, M. Leoky, and N. H. McClamroch, "Geometric tracking control of a quadrotor uav on se (3)," in *Decision and Control (CDC), 2010 49th IEEE Conference on*. IEEE, 2010, pp. 5420–5425.
- [31] F. Bullo and R. M. Murray, "Tracking for fully actuated mechanical systems: a geometric framework," *Automatica*, vol. 35, no. 1, pp. 17–34, 1999.
- [32] A. Y. Mersha, R. Carloni, and S. Stramigioli, "Port-based modeling and control of underactuated aerial vehicles," in *2011 IEEE Int. Conf. Robot. Autom.* IEEE, may 2011, pp. 14–19.
- [33] J. Acosta, M. Sanchez, and A. Ollero, "Robust control of underactuated aerial manipulators via ida-pbc," in *Decision and Control (CDC), 2014 IEEE 53rd Annual Conference on*. IEEE, 2014, pp. 673–678.
- [34] J. Acosta, C. de Cos, and A. Ollero, "A robust decentralised strategy for multi-task control of unmanned aerial systems. application on under-actuated aerial manipulator," in *Unmanned Aircraft Systems (ICUAS), 2016 International Conference on*. IEEE, 2016, pp. 1075–1084.
- [35] R. M. Murray, Z. Li, S. S. Sastry, and S. S. Sastry, *A mathematical introduction to robotic manipulation*. CRC press, 1994.
- [36] D. D. Holm, *Geometric Mechanics: Part II: Rotating, Translating and Rolling*. World Scientific Publishing Company, 2008.
- [37] R. Rashad, "Energy-based modeling and control of interactive aerial robots: A geometric port-hamiltonian approach," Ph.D. dissertation, University of Twente, 2021.
- [38] A. De Luca and R. Mattone, "Sensorless robot collision detection and hybrid force/motion control," in *Robotics and Automation, 2005. ICRA 2005. Proceedings of the 2005 IEEE International Conference on*. IEEE, 2005, pp. 999–1004.
- [39] A. De Luca, A. Albu-Schaffer, S. Haddadin, and G. Hirzinger, "Collision detection and safe reaction with the dlr-iii lightweight manipulator arm," in *Intelligent Robots and Systems, 2006 IEEE/RSJ International Conference on*. IEEE, 2006, pp. 1623–1630.
- [40] K.-S. Kim, K.-H. Rew, and S. Kim, "Disturbance observer for estimating higher order disturbances in time series expansion," *IEEE Transactions on automatic control*, vol. 55, no. 8, pp. 1905–1911, 2010.
- [41] M. Ryll, G. Muscio, F. Pierri, E. Cataldi, G. Antonelli, F. Caccavale, D. Bicego, and A. Franchi, "6D interaction control with aerial robots: The flying end-effector paradigm," *The International Journal of Robotics Research*, vol. 38, no. 9, pp. 1045–1062, 2019.
- [42] "20Sim 4.7, Controllab Products B.V." [Online]. Available: <http://www.20sim.com/>
- [43] F. Furrer, M. Burri, M. Achtelik, and R. Siegwart, "Rotors-a modular gazebo mav simulator framework," in *Robot operating system (ROS)*. Springer, 2016, pp. 595–625.
- [44] J. Zult, "Achieving stable and safe physical interaction for a fully actuated aerial robot using energy tank-based interaction control," Master's thesis, University of Twente, 2020.
- [45] R. Rashad, D. Bicego, R. Jiao, S. Sanchez-Escalonilla, and S. Stramigioli, "Towards vision-based impedance control for the contact inspection of unknown generically-shaped surfaces with a fully-actuated uav," in *2020 IEEE/RSJ International Conference on Intelligent Robots and Systems (IROS)*, 2020, pp. 1605–1612.